Fall 2017

Sparse emission source microscopy for rapid emission source imaging

Ling Zhang

Recommended Citation

SPARSE EMISSION SOURCE MICROSCOPY

FOR RAPID EMISSION SOURCE IMAGING

by

LING ZHANG

A THESIS

Presented to the Faculty of the Graduate School of the

MISSOURI UNIVERSITY OF SCIENCE AND TECHNOLOGY

In Partial Fulfillment of the Requirements for the Degree

MASTER OF SCIENCE IN ELECTRICAL ENGINEERING

2017

Approved by

Dr. David Pommerenke, Advisor
Dr. James Drewniak
Dr. Victor Khilkevich

PUBLICATION THESIS OPTION

This thesis consists of the following two articles:

Paper I: Pages 3-27 have been published by IEEE Transactions on Electromagnetic Compatibility.

Paper II: Pages 28-46 have been published by IEEE Transactions on Electromagnetic Compatibility.

ABSTRACT

In Paper I, Sparse Emission Source Microscopy (ESM) methodology will be introduced and discussed for the localization of major EMI radiation sources in complex and large systems. Traditional ESM method takes abundant and uniformly-distributed scanning points on the scanning plane using a robotic system, which can provide high-quality source images but consumes too much time. This section presents a sparse and nonuniform sampling technique for ESM, which is more time-efficient in identifying major radiation sources, even though the image quality is sacrificed. The feasibility of sparse sampling is mathematically proved, and it is shown that increasing number of points increases the signal-to-noise ratio (SNR) of reconstructed images. What's more, a nearest neighbor interpolation method is utilized to estimate the radiated power in real-time scanning. Thus, back-propagated images and estimated radiated power can be obtained in real-time measurement, which can efficiently and instantaneously provide the locations and the radiation strengths of the most significant emission sources.

In Paper II, EMI coupling paths and mitigation of optical transceiver modules are investigated. Optical transceiver modules are commonly used in telecommunication and data communication systems, and are significantly troublesome at their operation frequencies and/or harmonics. In this section, simulations and measurements are performed on optical transceiver modules, and total radiated power (TRP) is also measured, to identify and characterize the EMI coupling paths. Currents on the silicon photonic sub-assembly conductor housing and optical fiber connection ferrule are identified as a dominant radiating source. EMI mitigation methods are developed and shown to be effective in reducing the radiated emissions from real product hardware.

ACKNOWLEDGMENTS

TABLE OF CONTENTS

LIST OF ILLUSTRATIONS

Paper II

LIST OF TABLES

INTRODUCTION

With the continuous increase of the operating data rate in electronic products, electromagnetic interference (EMI) analysis is becoming more and more problematic in large and complex systems. Near-field electromagnetic scanning is a typical method for the localization of radiation sources in complex electronic systems. However, besides propagating fields that contribute to far-field radiation, which is what engineers are more concerned about in real applications, evanescent fields are also inevitably detected by near-field scanning method, which in most of the cases does not allow to correlate near-field and far-field measurements. Also because of the mechanical restrictions, near-field probes are unable to reach close enough to all locations and components. Emission Source Microscopy (ESM) technique which will be discussed in this work is an alternative solution for localization and characterization of active radiation sources by measuring the field magnitude and phase over a plane away from the device under test (DUT) and back-propagating the field onto the DUT plane. In previous work on ESM technique, dense and uniformly-distributed sampling points are picked on the scanning plane using a robotic scanning system. The separation between scanning points should be less than $\lambda/2$ in order to satisfy the Nyquist spatial sampling criterion. This way of obtaining field samples can provide high-quality images of radiation sources, but leads to long measurement time. Paper I presents a method of manually selecting sparse and nonuniform sampling points that is applied to the ESM technique. The proposed method is especially effective for the localization of the dominant radiation sources (when large SNR of the image is not needed) which are regarded as more significant by EMC engineers. At the same time, the overall source image quality is sacrificed. Moreover, a nearest neighbor interpolation method is applied to interpolate the field magnitude between the scanning points, so that the radiated power through the scanning plane can be estimated using Poynting's theorem. Therefore, reconstructed source images and radiated power through the scanning plane can be obtained in the real-time scanning process, providing information about the source locations and radiation strength in a time-efficient and effective fashion for the identification of the major EMI sources in a system.

The continuous increase of data rate in electronic products and network bandwidth has resulted in the widespread use of optical transceiver modules in Gigabit Ethernet systems, due to their high throughput of several hundred gigabits per second (Gbps). These modules are typically used in high-end and low-end switches and routers, and are located at the front-end of the system chassis. Electromagnetic interference (EMI) problems can result from these modules at their operation frequency and/or harmonics. In paper II, in order to further quantitatively investigate the EMI coupling paths on the optical transceiver module, measurements and full-wave simulations were performed on the optical subassembly package to compare total radiated power (TRP) variations with absorbing material covering different regions. The comparison of the contributions to TRP from different parts of the signal path demonstrated that the connector from the transceiver circuit board to the flex cables in the OSA, and the flex cables connecting the transceiver circuit board to the electrical-to-optical interface assembly are two dominant coupling paths at high frequencies above 10 GHz. Paper II utilizes full-wave EM simulation to investigate the coupling paths that contribute to the propagating modes of the electromagnetic field within the cage that illuminates slots, and the silicon photonics conducting enclosure. The EMI coupling paths from these interior sources to the apertures on the outside enclosure and the electrical-to-optical interface assembly conductor packaging are demonstrated through simulation and measurement. Mitigation methods using absorbing materials to load the coupling paths are demonstrated to be effective in suppressing the radiation from the OSA. Application of absorbing material and conducting O-rings to mitigate the radiated emissions from real products provides corroboration for the identified EMI coupling paths as well as the EMI mitigation methods for the optical transceiver modules in real product applications.

PAPER

I. SPARSE EMISSION SOURCE MICROSCOPY FOR RAPID EMISSION SOURCE IMAGING

ABSTRACT

Emission Source Microscopy (ESM) technique can be utilized for the localization of EMI sources in complex and large systems. This paper presents a sparse and nonuniform sampling technique for ESM. Compared with the traditional way of acquiring abundant and uniformly-distributed scanning points on the scanning plane using a robotic scanning system, the proposed method is much more time-efficient in identifying the major radiation sources, even though the image quality is sacrificed. The feasibility of sparse sampling is mathematically proved, and it is shown that increasing number of scanning points increases the signal-to-noise ratio (SNR) of reconstructed images. Besides, a nearest neighbor interpolation method is applied in the real-time processing to estimate the radiated power through the scanning plane. Thus, back-propagated images and estimated radiated power can be obtained in the real-time measurement process, which can efficiently and instantaneously provide the locations and the radiation strength of the most significant emission sources.

1. INTRODUCTION

With the continuous increase of the operating data rate in electronic products, electromagnetic interference (EMI) analysis is becoming more and more problematic in large and complex systems. Near-field electromagnetic scanning is a typical method for the localization of radiation sources in complex electronic systems [1]-[4]. However, besides propagating fields that contribute to far-field radiation, which is what engineers are more concerned about in real applications, evanescent fields are also inevitably detected by near-field scanning method, which in most of the cases does not allow to correlate near-

field and far-field measurements. Also because of the mechanical restrictions, near-field probes are unable to reach close enough to all locations and components.

Emission Source Microscopy (ESM) technique which will be discussed in this work is an alternative solution for localization and characterization of active radiation sources by measuring the field magnitude and phase over a plane away from the device under test (DUT) and back-propagating the field onto the DUT plane [5]-[7]. Similar ideas have been used in the form of the synthetic aperture radar (SAR) technique for antenna diagnostics and antenna pattern measurements [8]-[10] as well as for microwave imaging to detect concealed objects and structural defects [11], [12].

In previous work on ESM technique [5]-[7], dense and uniformly-distributed sampling points are picked on the scanning plane using a robotic scanning system. The separation between scanning points should be less than $\lambda/2$ in order to satisfy the Nyquist spatial sampling criterion [13]. This way of obtaining field samples can provide high-quality images of radiation sources, but leads to long measurement time.

To minimize the number of required spatial samples in SAR method, measurement techniques taking sparse and non-uniform samples have been proposed to get real-time SAR images, despite some image artifacts as a result of sparsely measured data [14].

Based on the work of [14], this paper presents a similar method of manually selecting sparse and nonuniform sampling points that is applied to the ESM technique. Furthermore, it is mathematically proven that increasing number of samples proportionally increases the signal-to-noise ratio (SNR) of reconstructed image for an ideal point source, allowing to select the number of samples based on the desired image accuracy. This result allows obtaining images of acceptable quality just by a proper choice of number of samples and without any special data treatment such as non-uniform Fourier transform and compressed sensing [15]-[17]. The proposed method is especially effective for the localization of the dominant radiation sources (when large SNR of the image is not needed) which are regarded as more significant by EMC engineers. At the same time, the overall source image quality is sacrificed.

Moreover, a nearest neighbor interpolation method is applied to interpolate the field magnitude between the scanning points, so that the radiated power through the scanning plane can be estimated using Poynting's theorem. Therefore, reconstructed source images

and radiated power through the scanning plane can be obtained in the real-time scanning process, providing information about the source locations and radiation strength in a time-efficient and effective fashion for the identification of the major EMI sources in a system.

2. SPARSE EMISSION SOURCE MICROSCOPY ALGORITHM

In the ESM system setup, two antennas are needed to get the field magnitude and phase on the scanning plane, among which Antenna A is moved on the scanning plane, and Antenna B is fixed to obtain a phase reference, as shown in Fig. 1. Signals from Antenna A and B are fed into the ports of a vector network analyzer (VNA) operating in tuned receiver mode. Two position encoders are used to measure the position of Antenna A.

This section briefly introduces the algorithm of 2D ESM scanning first, after which the relationship between the number of samples and the image quality of sparse ESM is mathematically derived and analyzed. Then the feasibility of sparse ESM is validated through numerical simulations.
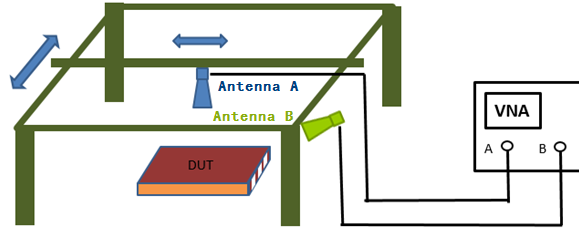
Figure 1. ESM system schematic.

2.1. 2D ESM Algorithm

The ESM algorithm is based on the SAR technique, which depends on a two-dimensional (2D) Fourier transform, and can be summarized through the following equation [6]:

$$E_t^0(x, y, 0) = \mathcal{F}^{-1}\left[\mathcal{F}\{E_t(x, y, z_0)\} \cdot e^{jk_z z_0}\right] \tag{1}$$

The assumption of (1) is that the scanning and source planes are both parallel to the x-y plane, and z_0 is the distance between these two planes. $E_t(x, y, z_0)$ and $E_t(x, y, 0)$ are the tangential fields on the scanning and source planes respectively. $k_z = \sqrt{k^2 - k_x^2 - k_y^2}$ is the z component of the propagation vector, where k_x, k_y are the x and y components of propagation vector, and k is the free space wavenumber [1]. k_x and k_y are also the spatial frequencies of 2D Fourier transform. $\mathcal{F}$ and $\mathcal{F}^{-1}$ are the forward and reverse Fourier transform operators respectively. If the fast Fourier transform algorithm is used, even with millions of samples the ESM transformation can be performed within a fraction of second, which makes real-time operation applicable.

2.2. Mathematical Feasibility of Sparse ESM

The analysis below is performed for the 1-dimensionsal (1D) case, which can be easily generalized to a 2D situation.

Let us assume that the signal on the scanning plane is a harmonic function $g(x)$ with the frequency ω_0 and unit magnitude: $g(x) = e^{j\omega_0 x}$. Suppose that $g(x)$ is sampled at random locations $x_1, x_2, \dots, x_N$, where N is the number of samples. The sampling process can be described as a summation of the products of the $g(x)$ with delta functions randomly shifted to the locations x_i resulting in the sampled function $g_s(x)$:

$$g_s(x) = g(x) \sum_{i=1}^{N} \delta(x - x_i) = e^{j\omega_0 x} \sum_{i=1}^{N} \delta(x - x_i) \tag{2}$$

After applying the continuous Fourier transform on the sampled function $g_s(x)$, the spectrum of $g_s(x)$ is given by:

$$
\begin{aligned}
G_s(\omega) &= \mathcal{F}\left(e^{j\omega_0 x} \sum_{i=1}^{N} \delta(x - x_i)\right) \\
&= \sum_{i=1}^{N} \mathcal{F}\left(e^{j\omega_0 x} \delta(x - x_i)\right)
\end{aligned}
\tag{3}
$$

From convolution theorem,

$$G_s(\omega) = \sum_{i=1}^{N} \mathcal{F}\left(e^{j\omega_0 x}\right) * \mathcal{F}\left(\delta(x - x_i)\right)$$

$$= \sum_{i=1}^{N} \delta(\omega - \omega_0) * e^{-j\omega x_i} = \sum_{i=1}^{N} e^{-j(\omega - \omega_0) x_i} \qquad (4)$$

From (4), it can be seen that the spectrum of the randomly sampled harmonic function is a summation of complex exponentials with random frequencies corresponding to the random sampling positions. At the frequency $\omega = \omega_0$, values of all exponentials are equal to 1. So the absolute value at $\omega = \omega_0$ in the spectrum is $|G_s(\omega_0)| = N$. At all other frequencies, the summation of N uncorrelated harmonic functions with unit amplitudes is performed. Since the standard deviation of each harmonic function is equal to 1, according to the central limit theorem [18], the summation of N independent harmonic function (if N is a large number) will follow an approximate normal distribution, of which the standard deviation is $\sqrt{N}$ and the variance is N.

The analysis above shows that a random signal will be generated at all frequencies except ω_0. For convenience this signal is called noise in this paper (the noise due to the random sampling should not be confused with the measurements noise due to the limited signal-to-noise ratio of the instrument and other factors such as sampling antenna positioning accuracy). The spectrum peak value at frequency $\omega = \omega_0$ is the desired signal.

The signal-to-noise ratio (SNR) for the spectrum of a sparsely sampled harmonic function is defined as the ratio of signal power to the noise variance (average noise power), which is

$$SNR_{(one\ harmonic)} = \frac{Signal\ power}{Noise\ variance} \approx \frac{N^2}{N} = N \qquad (5)$$

The conclusion in (5) is based on the analysis in continuous Fourier transform. Since discrete Fourier transform is in a certain sense an approximation for continuous Fourier transform, so the conclusion in (5) also applies in discrete Fourier transform (DFT). The difference is that the frequencies are discretely distributed in DFT. The precondition

for the conclusion in (5) is that the number of sparse samples is much less than the total number of original uniformly sampled field. Indeed if the number of sparse samples is equal to the number of uniform samples, the sparse sampling noise is absent and the SNR of the signal is infinite, which clearly contradicts (5). On practice, however, the number of sparse samples is quite low relative to the number of uniform samples, otherwise the sparse sampling would have little advantage over the uniform one.

(a)   (b)
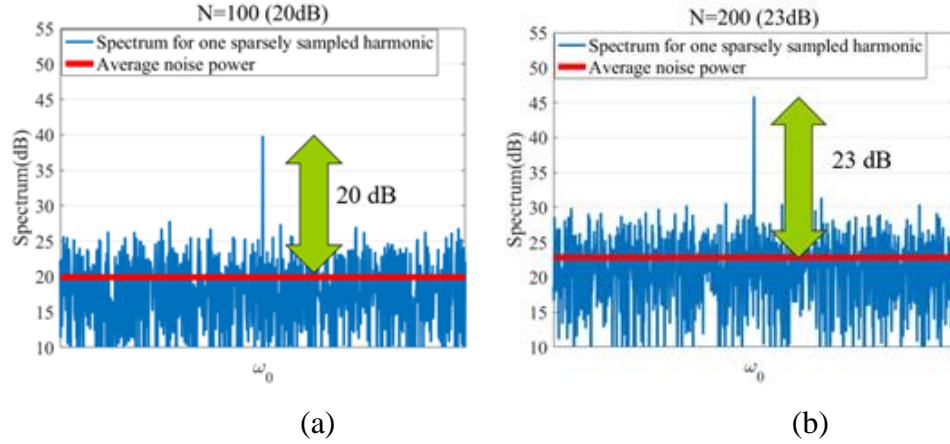
Figure 2. Numerical simulation for the spectrum of one sparsely sampled harmonic function. (a) When N = 100, simulated SNR is 20 dB, which agrees with the calculation according to (5). (b) When N= 200, simulated SNR is 23 dB, which also agrees with (5). The averaged noise power was obtained by averaging over many random sampling distributions.

Fig. 2 shows the numerical simulation results for the DFT of a sparsely sampled harmonic function $g(x) = e^{j\omega_0 x}$ for different number of samples. The simulated SNR results match well with the estimation using (5).

The idealized spatial frequency spectrum (uniform on the interval from –k to k, and zero outside the region) for a point source is shown in Fig. 3 (a) (the actual point source spectrum is not uniform, but is reasonably close to the rectangular one – the rectangular spectrum is introduced here to simplify the analysis). The image of the point source with the idealized spectrum is a sinc function (Fig. 3 (b)), as it is represented by the inverse Fourier transform (see (1)). Assume that the scanning range in spatial domain is from $-L$ to L, within which there are N_{tot} uniformly distributed scanning points. From the

properties of DFT, the intervals between the frequency samples in the spectrum is dependent on the scanning range in spatial domain, namely

$$\Delta k = \frac{2\pi}{2L} = \frac{\pi}{L} \qquad (6)$$

Suppose there are M frequencies on the interval $[-k, k]$, then

$$M = \frac{2k}{\Delta k} = \frac{2kL}{\pi} \qquad (7)$$
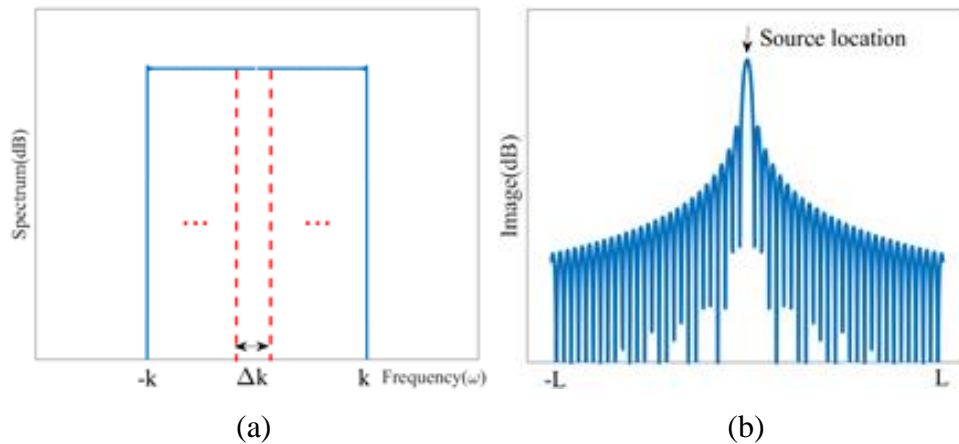
Figure 3. (a) Idealized frequency spectrum of an image source. (b) Idealized point source image.

As is analyzed above, every frequency component between $-k$ to k will also generate noise on other frequencies due to sparse sampling, which means the noise from different frequencies will add up together. Assuming that the noises from different frequencies are uncorrelated with each other, the standard deviation of the resulting noise can be calculated as $\sqrt{MN}$, which gives the noise variance (average noise power) on the interval from $-k$ to k equal to MN due to the summation of the noise from different frequencies.

A simple numerical simulation is performed to verify this approximation, as shown in Fig. 4. Based on Fig. 2 (b), four harmonic functions with the same amplitude are added together, and 200 sparse samples are taken randomly. It can be seen from Fig. 4 that the

average noise power increases for about 6 dB compared with the result in Fig. 2 (b), which verifies the reasonableness of the assumption made above.
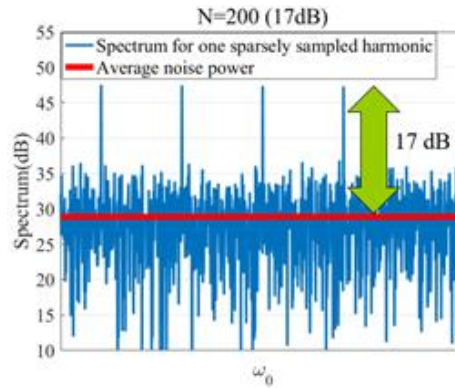
Figure 4. 200 sparse random samples are taken in the sum of four harmonic functions with the same amplitude. The average noise power increases for about 6 dB compared with Fig. 2 (b).

During imaging both the signal and the sampling noise undergo the transformation according to (1). The image due to the signal always produces a sinc function as illustrated by Fig. 3. The transformation of the noise is more complicated. Numerical simulation shows that in general the variance of the noise is not constant on the interval $[-L, L]$, and strongly depends on the aperture angle. The aperture angle is defined as shown in Fig. 5. As can be seen from the Fig. 6, the noise variance becomes almost flat if the aperture angle is less than 45 degrees. At the same time the noise levels at large distances from the source locations increases with the decrease of the aperture angle. Therefore, the flat noise distribution can be regarded as the worst case (since false sources at large distances from the real one are especially detrimental) and is analyzed henceforth.

Fig. 7 shows the diagram for the spectrum and image with sparse sampling. $H_1(\omega)$ is the idealized spectrum of a single point source, which has uniform amplitude from $-k$ to k, i.e.

$$|H_1(\omega)|^2 = \begin{cases} 1, -k \leq \omega \leq k \\ 0, \text{otherwise} \end{cases} \qquad (8)$$
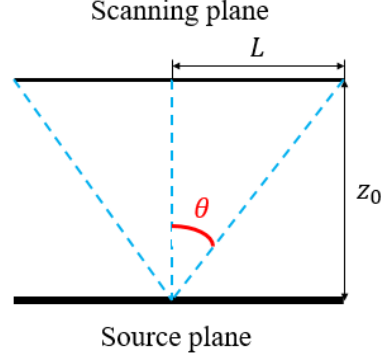
Figure 5. The definition of the aperture angle θ: $tan\theta = L/z_0$.

(a)   (b)
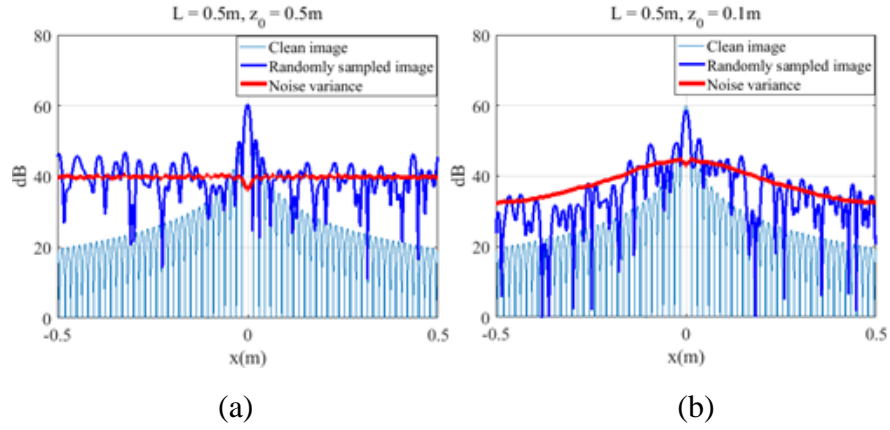
Figure 6. Aperture angle will influence the noise distribution. (a) When $L = 0.5\,m, z_0 = 0.5\,m$ ($\theta = 45°$), the noise distribution is almost flat. (b) When $L = 0.5\,m, z_0 = 0.1\,m$, the distribution is not flat, approaching the envelope of the sinc function at z0=0 (infinite θ). The noise level far away from the source location becomes lower as the aperture angle increases.

$h_1(\omega)$ is the noise added by the sparse sampling. $\overline{|h_1(\omega)|^2}$ is used to represent the average noise power from $-k$ to k, where the bar represents averaging over realizations (images calculated with different distribution of samples). As has been analyzed before, the ratio of the signal to the average power of noise between $-k$ to k should be approximately equal to

$$SNR_{spectrum} = \frac{|H_1(\omega)|^2}{\overline{|h_1(\omega)|^2}} \approx \frac{N^2}{MN} = \frac{N}{M} \tag{9}$$

From (7) and (9), the SNR of the spectrum between $-k$ to k is calculated to be

$$SNR_{spectrum} = \frac{|H_1(\omega)|^2}{|h_1(\omega)|^2} \approx \frac{N\pi}{2kL} \tag{10}$$

In the image, $H_2(x)$ is used to represent the idealized image (a sinc function). According to the Fourier transform, it is not difficult to calculate the expression of $|H_2(x)|$ to be

$$|H_2(x)| = \frac{k}{\pi} \cdot \left|\frac{\sin(kx)}{kx}\right| = \frac{k}{\pi} \cdot \left|sinc\left(\frac{k}{\pi}x\right)\right| \tag{11}$$

$h_2(x)$ stands for the noise in the image due to sparse sampling. The average power of $h_2(x)$ can be calculated from $h_1(\omega)$ using Parseval's theorem:

$$\int_{-k}^{k} |h_1(\omega)|^2 \frac{d\omega}{2\pi} = \int_{-L}^{L} |h_2(x)|^2 dx \tag{12}$$

(a)   (b)
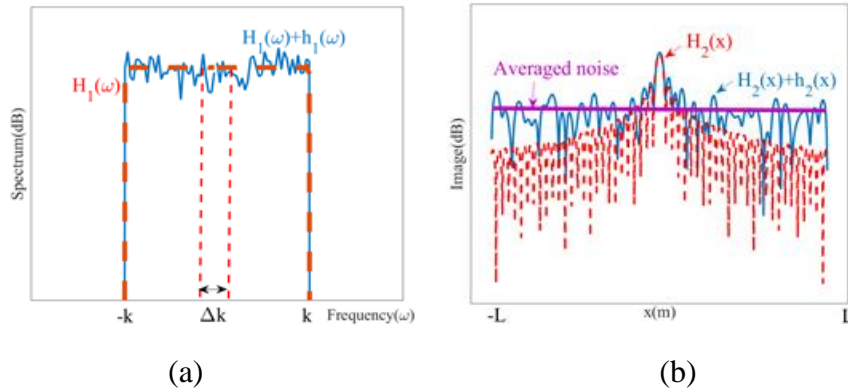
Figure 7. Diagram of 1D sparse sampling. (a) Frequency spectrum. $H_1(\omega)$ is the idealized spectrum for a single source. $H_1(\omega) + h_1(\omega)$ is the spectrum for sparsely sampled source field, where $h_1(\omega)$ is the spectrum noise due to sparse sampling. (b) Source image. $H_2(x)$ is the idealized image for a single source. $H_2(x) + h_2(x)$ is the reconstructed image using sparse sampling, where $h_2(x)$ is the image noise due to sparse sampling.

(12) can be simplified to (13) assuming flat distributions of the noise power in frequency and spatial domains:

$$\overline{|h_1(\omega)|^2} \cdot 2k \cdot \frac{1}{2\pi} = \overline{|h_2(x)|^2} \cdot 2\text{L} \tag{13}$$

The average SNR in the image due to sparse sampling is defined as the ratio of the power of the signal peak to the average noise power in the image (again assuming a flat noise distribution):

$$SNR_{avg} = \frac{\max(|H_2(x)|^2)}{\overline{|h_2(x)|^2}} = \frac{k^2/\pi^2 \cdot |H_1(\omega)|^2}{\overline{|h_2(x)|^2}} \tag{14}$$

Finally by combining (10), (13), and (14), the average SNR in the image for a sparsely-sampled point source field can be calculated as follows:

$$SNR_{avg} = N \tag{15}$$

Similar to (5), the precondition for the conclusion in (15) is that the number of sparse samples is much less than the total number of original uniform samples for a point source field. This condition also agrees with the way that samples are taken in the real measurements of sparse ESM method.

The definition of noise level in the SNR of (15) is the average noise power. However, in real applications, the highest possible noise level which may be confused with existing sources is more significant. As has been analyzed, the noise distribution in the spectrum follows normal distribution. According to three-sigma rule for the normal distribution with unit variance, the highest possible noise level with 99.7% probability is no more than nine times of the average noise power. This gives the following result for the minimum SNR of the image defined as the ratio of the image peak to the noise peak:

$$SNR_{min} = N/9 \tag{16}$$

2.3. Simulation Validation of Sparse ESM

To verify the approximation of SNR in (15) and (16), 1D and 2D numerical simulations were performed. The field generated by the Hertzian dipole was calculated along a line or on a plane and then randomly sampled with variable number of samples. The obtained SNR levels of the images are presented in Fig. 8. The simulated SNR_{avg} and SNR_{min} are compared with the estimated SNR_{avg} and SNR_{min} as the number of samples increases. For each number of samples, the estimated SNR_{avg} and SNR_{min} are calculated from (15) and (16) respectively; the simulated SNR_{avg} is obtained by calculating the statistical average value of noise for different positions of the samples. Similarly, the simulated SNR_{min} is obtained by calculating the statistical average value of the highest noise level.
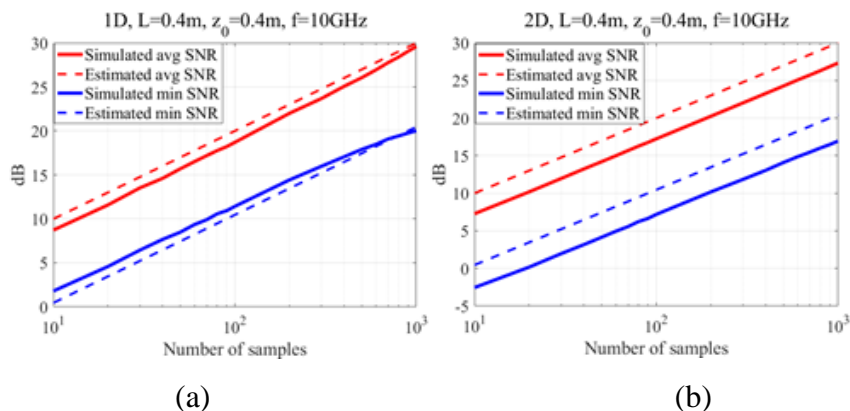
Figure 8. (a) Sparse sampling of the radiation field of the Hertzian dipole in 1D case. Total number of points $N_{tot} = 5000$. $L = 0.4\,m, z_0 = 0.4\,m, f = 10\,GHz$. (b) Sparse sampling of the radiation field of a dipole in 2D case. Total number of points $N_{tot} = 40000$. $L = 0.4\,m, z_0 = 0.4\,m, f = 10\,GHz$.

As can be seen from Fig. 8, the SNR of the images is proportional to the number of samples in both 1D and 2D cases. There is however a discrepancy in the predicted levels. The difference might be due to the deviation of the actual spatial spectrum of the dipole source from the idealized form (8). The magnitude of the actual spectrum decreases close to the edges on the non-zero interval which is in turn always narrower than [-k, k] due to the limited scanning aperture (see example in Fig. 9). Nevertheless, the accuracy of the SNR estimations is good enough for many EMC applications (not worse than 3 dB).

The mathematical derivations given above and numerical simulations have verified that increasing number of sparse samples can linearly increase the SNR in the image, which corroborates the theoretical feasibility of sparse ESM method.

On the other hand, the amplitude of the ESM image strongly depends on the number of samples and their locations. The next section proposes a method for the total radiated power measurement and the corresponding image amplitude correction.

| (a) | (b) |
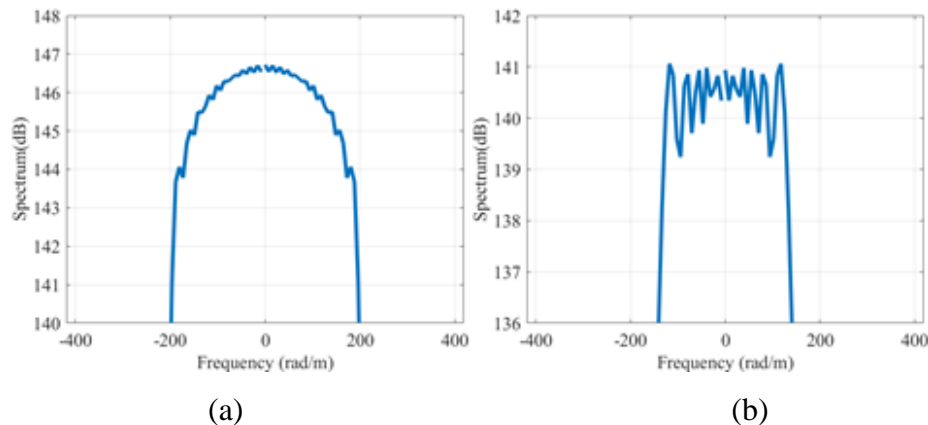
Figure 9. Two examples of the 1D spatial spectrum for a Hertzian dipole source at 10 GHz, when $k \approx 209 \, rad \cdot m^{-1}$. (a) $N_{tot} = 5000, L = 0.4 \, m, z_0 = 0.1 \, m$. (b) $N_{tot} = 5000, L = 0.4 \, m, z_0 = 0.4 \, m$.

3. RADIATED POWER CALCULATION

When scanning points are uniformly distributed, comparisons between different cases, e.g. without absorbing material and with absorbing material, can be made directly [7]. However, when scanning points are sparsely and non-uniformly distributed, different number of samples can lead to different peak values in the source field images, which makes the absolute field values of source images unreliable. In order to provide a reference value for the radiation strength of sources, this paper makes use of a nearest neighbor interpolation method to calculate the radiated power through the scanning plane.

3.1. Nearest Neighbor Interpolation Method

Nearest neighbor interpolation method is an interpolating technique where the domain of the interpolant is divided into a set of points closest to the sample locations and then values of the samples are assigned to all points within corresponding areas [19]. Fig. 9 shows an example of how this function works. The small circles represent the scanned points. Every polygon in Fig. 9 that contains a scanned point stands for the region that contains the points closest to this particular point. The polygons are found using the Voronoi partitioning algorithm [20].
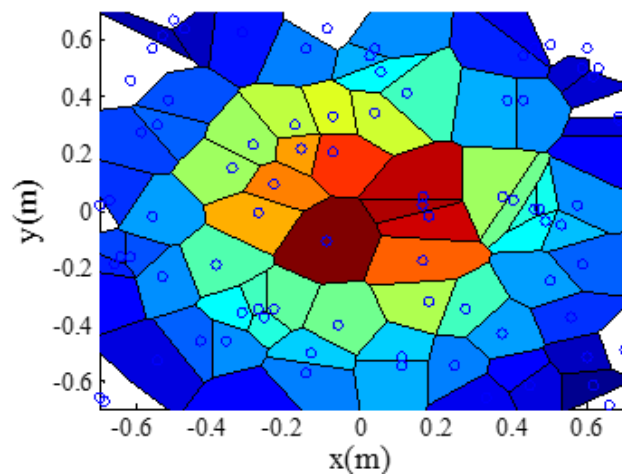
Figure 10. An example of nearest neighbor interpolation.

To perform the ESM transformation and the power interpolation a dense and uniform grid of coordinates is created first along with the corresponding matrix to store the acquired E field values. Initially all elements of the matrix are set to zero. Each time a sample of the electromagnetic field is obtained and written to the matrix, the nearest neighbor interpolation is used to interpolate the E field magnitudes at all grid nodes. Thus the radiated power of the tangential field through the scanning plane can be calculated through the integration over the scanning plane area A according to Poynting's theorem,

$$P_{tot} = \iint_A \frac{|E|^2}{2\eta} ds = \sum_i \frac{|E_i|^2}{\eta} A_i \qquad (17)$$

where η is the free space wave impedance; E_i is the field at sampling location i and A_i is the area of the corresponding nearest neighbor region.

Based on the estimation of P_{tot} through nearest neighbor interpolation, an empirical equation (18) as follows has been found to be able to roughly normalize the E field magnitude of the image accordingly, regardless of the number of samples.

$$|E_{tot}| = \frac{P_{tot}}{P_{sparse}} \cdot |E_{sparse}| \tag{18}$$

where $|E_{sparse}|$ is the magnitudes of the reconstructed E field on the scanning plane using the sparse samples and equation (1); $|E_{tot}|$ is the normalized E field magnitude on the scanning plane; and the power of the sparse image P_{sparse} is calculated as follows:

$$P_{sparse} = \sum_i \frac{|E_i|^2}{2\eta} \cdot \Delta x \cdot \Delta y \tag{19}$$

where Δx and Δy are the resolutions of the predefined grid. Thus the P_{sparse} can be understood as the radiated power of the sampled points only. Using equation (18) the E field magnitude in the image can be normalized regardless of number of samples, which provides another reference value for the radiation strength of sources besides the estimated power through the scanning plane.

3.2. Measurement Validation

To validate the proposed method of predicting the radiated power through the scanning plane in practice, a measurement has been designed to measure a known radiated power. To achieve this two 8.2-12.4 GHz standard gain horn antennas, of which Antenna B is used as a transmitter (source) and Antenna A is used as a receiver, are utilized in this measurement, as shown in Fig. 10. Antenna B is in a fixed position, and Antenna A can be moved in two directions. The polarization directions of Antenna A and Antenna B are the same, both parallel to the scanning plane.

The vertical distance between the apertures of the two antennas is 0.3 m. The dimension of the scanning plane is 0.8m × 0.8m. The separation between the predefined grid nodes is set to 1 mm. Antenna A and Antenna B are connected to Port 2 and Port 1 of a VNA respectively. S_{21} is measured to get the field magnitude and phase in every scanning point at 10 GHz.
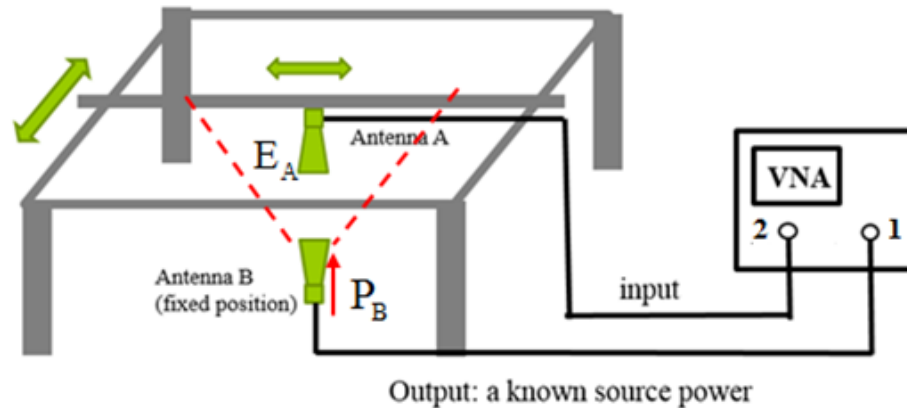
Figure 11. Measurement setup diagram for validating nearest neighbor interpolation method in calculating the radiated power through the scanning plane.

The following assumptions are made to perform the calculations below: a) the reflected power from Antenna B to Port 1 is negligible, which means that all the power which comes out from Port 1 is radiated out from Antenna B (this is a relatively accurate estimation because the reflection coefficient of the antenna is –18 dB at 10 GHz); b) polarization directions of Antenna A and Antenna B are perfectly parallel with each other; and c) the scanning plane is big enough, so that all the radiated power from Antenna B propagates through the scanning area. Also it is assumed that the incident voltage amplitude in the Antenna B port is 1 V. In a 50 Ω system, the time-averaged input (and hence radiated) power in this case will be

$$P_B = \frac{1^2}{50} \times \frac{1}{2}\ W = \left[10 \times log_{10}\left(\frac{1}{50} \times \frac{1}{2}\right) + 30\right] dBm$$

$$\approx 10\ dBm$$

(20)
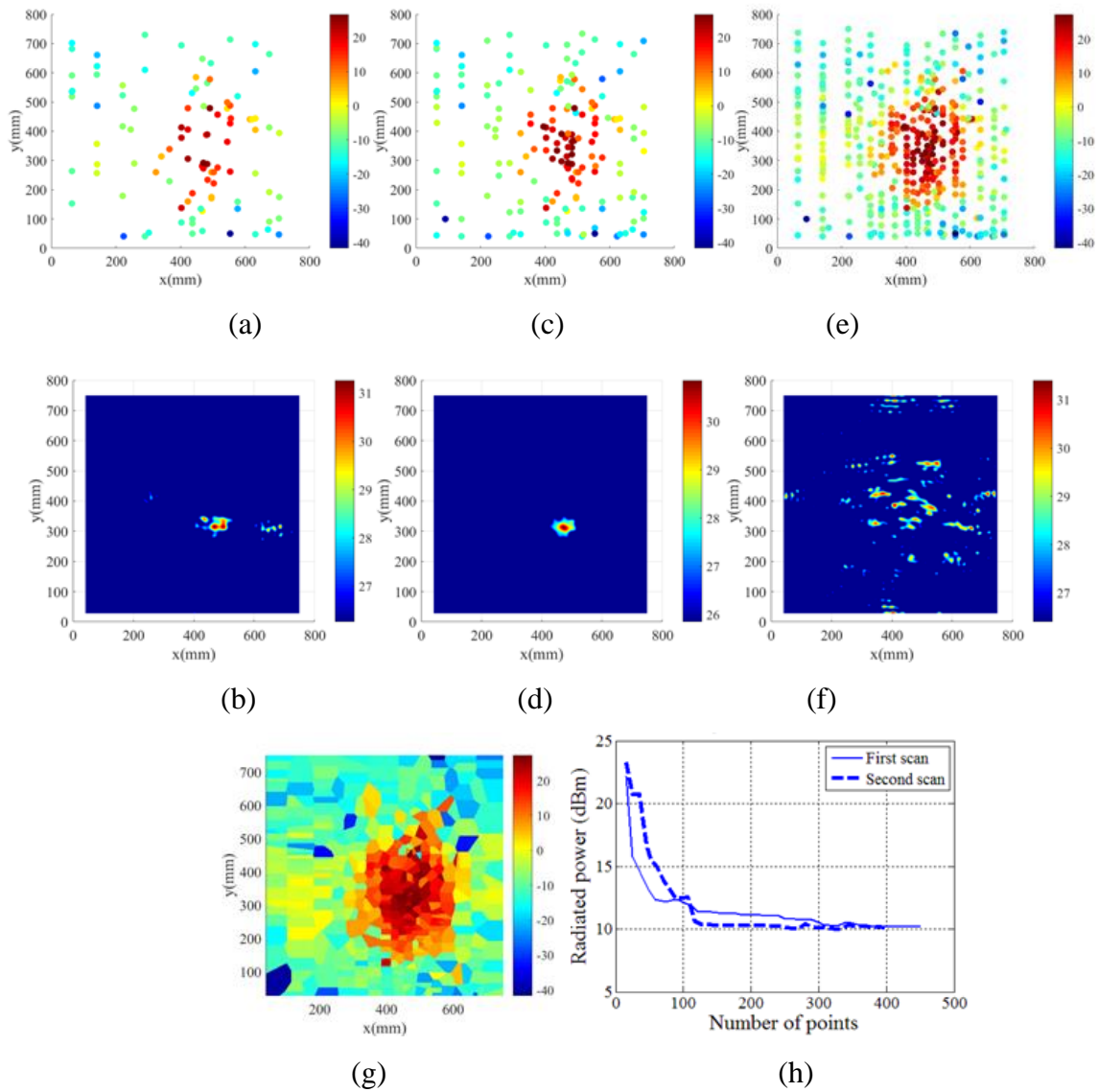
Figure 12. (a) E field magnitude of scanned points on the scanning plane when N = 100. (b) Reconstructed image on the image plane when $N = 100$. $E_{max} = 31.4\ dB(V/m)$. (c) E field magnitude of scanned points on the scanning plane when $N = 200$. (d) Reconstructed image on the image plane when $N = 200$. $E_{max} = 31.2\ dB(V/m)$. (e) E field magnitude of scanned points on the scanning plane when $N = 454$. (f) Reconstructed image on the image plane when $N = 454$. $E_{max} = 30.9\ dB(V/m)$. (g) E field magnitude on the scanning plane after using nearest neighbor interpolation when $N = 454$. (h) Convergence of calculated radiated power as a function of number of samples.

At every scanning point, the E field that Antenna A measures can be calculated using the antenna factor AF of antenna A:

$$E_A = 1V \cdot S_{21} \cdot AF = S_{21} \cdot AF \ (V/m) \tag{21}$$

Fig. 11 (a) to Fig. 11 (f) illustrate how the image quality changes when the number of sparse samples increases. The E field magnitude at the scanned points when $N = 100; \ 200; \ 454$ are shown in Fig. 11 (a), (c), (e) respectively (dot color corresponds to the field strength), while Fig. 11 (b), (d), (f) show the corresponding reconstructed images. Fig. 11 (b) (d) (f) are plotted with the same dynamic range of 5 dB to make it easy to compare the image qualities.

When $N = 100$, some hot spots can already be found in the image. However, the image quality is still poor since the scanning points are too sparse. When N increases to 200, a strong radiation source has appeared. After more samples are added in the strongly-radiated region, a strong peak in the image is observed, which corresponds to the location of the source antenna.

Meanwhile, Fig. 11 (g) shows the magnitude of the E field on the scanning plane obtained using the nearest neighbor interpolation for $N = 454$. Fig. 11 (h) provides the convergence of calculated radiated power through the scanning plane as the number of scanning points increases. Two curves in Fig. 11 (h) representing two separate scans, both converging to the same expected value of 10 dBm, which demonstrates the accuracy and repeatability of the interpolation technique. Besides, the maximum E field in the image calculated by (18) in Fig. 11 (b, d, f) are 31.4 dB(V/m), 31.2 dB(V/m), 30.9 dB(V/m) respectively, which has a good stability as well.

4. APPLICATION ON REAL PRODUCTS

From the analysis and measurements above, it has been demonstrated that the sparse ESM method can be utilized for the localization of dominant radiation sources in a system with controlled signal-to-noise ratio. Moreover, the radiated power through

scanning plane as well as the maximum values of the ESM images can be estimated from sparse scanning points using the nearest neighbor interpolation of the magnitude. In the next section the measurements on a real product are presented to validate the practicality of this technique in real applications.

4.1. DUT for Measurement

The DUT used for validation is an off-the-shelf networking device with default software configuration installed [7]. There are 16 optical transceiver modules working on the device, as is shown in Fig. 12 (a). Each channel uses a dedicated frequency around 10.3 GHz, producing 15 radiation peaks in the EMI spectrum shown in Fig. 12 (b) (there are two channels working at the same frequency). The EMI spectrum in Fig. 12 (b) is obtained in a reverberation chamber (RC) as described in [21], [22] and will be used later to validate the proposed sparse ESM technique. This paper presents the application of sparse ESM on a single frequency i.e. frequency # 11 at 10.312558 GHz. Similarly, other frequencies can also be scanned and analyzed.

(a)   (b)
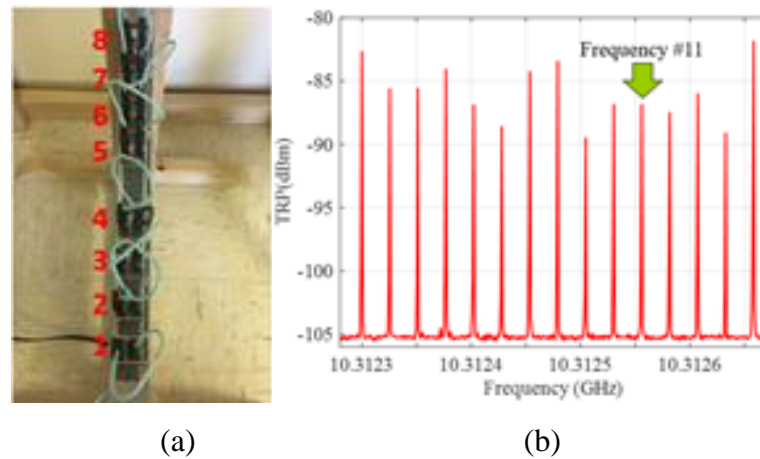
Figure 13. (a) Validation DUT with 16 optical transceiver modules (numbered by pairs). (b) 15 radiation peaks from the DUT around 10.3125 GHz.

4.2. Scanning Results on DUT

      The measurement setup diagram is shown in Fig. 1. Two 8.2-12.4 GHz standard gain horn antennas are used for scanning (antenna A) and obtaining the phase reference (antenna B). Similar to part B in section III, the dimension of the scanning plane is about 0.8m × 0.8m and the separation between the predefined scanning positions is 1 mm (resulting in about 640,000 points). The vertical distance from the bottom edge of Antenna A to DUT front panel is about 38 cm. In this paper, only the measurement of one component of the field is presented, which is perpendicular to the long side of the DUT. The measurement of the other component of the field can be performed similarly. The scanning results at frequency # 11 are shown in Fig. 13.

(a)   (b)

(c)   (d)
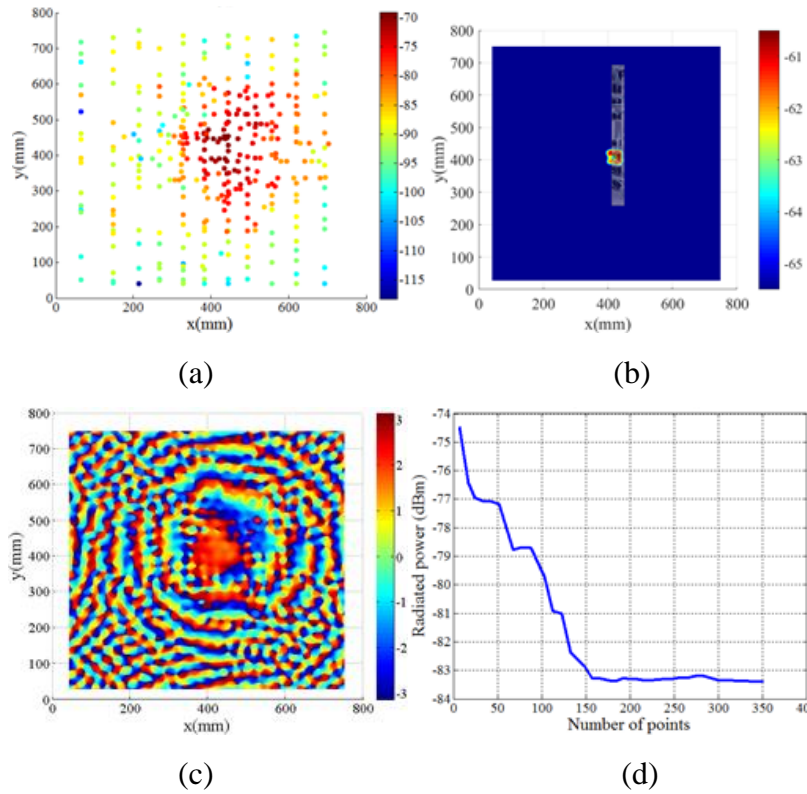
Figure 14. Scanning result at frequency # 11. (a) E field on the scanning plane. (b) Magnitude of reconstructed image on DUT plane. $E_{max} = -60.5 \, dB(V/m)$. (c) Phase of reconstructed image on DUT plane. (d) Convergence of calculated radiated power as a function of the number of samples. The converged radiated power is -83.4 dBm. Number of scanning points is 352.

23
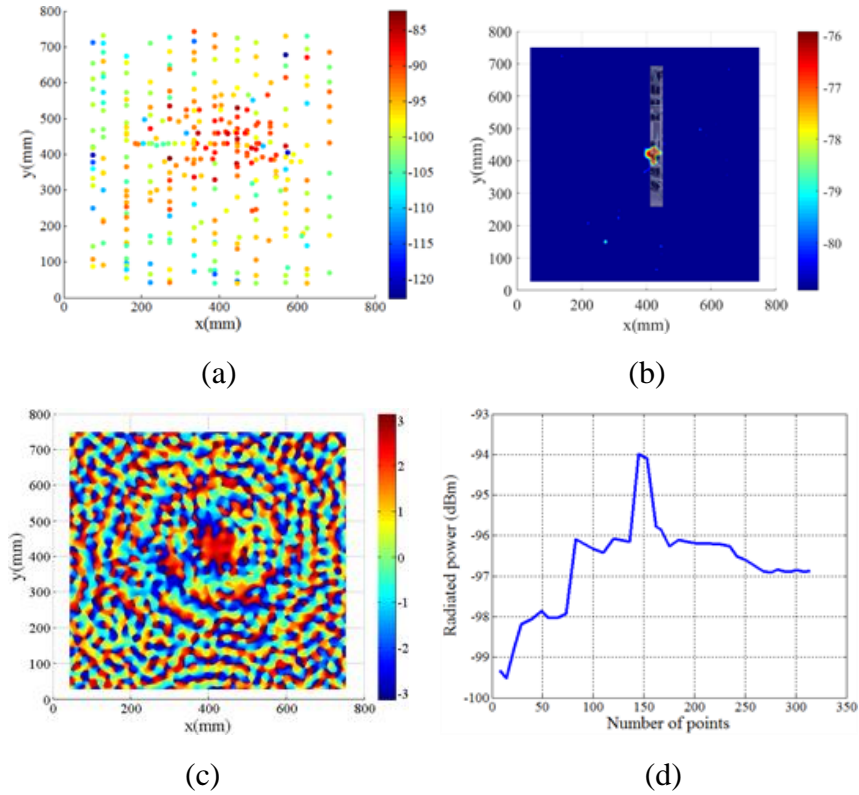
Figure 15. Scanning result at frequency # 11 after removing the corresponding radiated pair # 3. (a) E field on scanning plane. (b) Magnitude of reconstructed image on DUT plane. $E_{max} = -75.9\ dB(V/m)$ (c) Phase of reconstructed image on DUT plane. (d) Convergence of calculated radiated power with the increase of number of samples. The converged radiated power is -96.9 dBm. Number of scanning points is 314.

Table 1. Power comparison at frequency # 11.

	Power estimation through scanning plane	TRP measured in the RC
Power with pair # 3 (dBm)	-83.4	-86.9
Power without pair # 3 (dBm)	-96.9	-101.0
Power reduction (dB)	13.5	14.1

There are 352 scanning points in Fig. 14 (a). The E field magnitude at every scanning point does not represent the absolute value of the field at the scanning antenna location, since the cable loss, the amplifier gains, and the antenna factor are not taken into

account in the plots (however, all these factors are accounted for in the total radiated power calculation), therefore the plots in Fig. 14 (a and b) represent the relative values, which however is sufficient for the present analysis. The photographic image of the DUT is overlapped and aligned with the ESM image for the localization of radiation sources. Fig. 14 (b) shows that the hot spot overlaps with pair # 3, revealing the location of the EMI source. Also, from the phase of reconstructed image in Fig. 14 (c), it can be seen that the source is located in the center of phase contour lines as expected. In Fig. 14 (d), the calculated radiated power begins to converge when number of samples reach approximately 150. The calculated radiated power through the scanning plane is finally estimated as -83.4 dBm.

In order to verify the ability of the sparse ESM to locate the source and measure the radiated power, the identified module was removed from the DUT, and the scan was performed again, the results of which are shown in Fig. 15. From Fig. 15 (a), it can be seen that the E field on the scanning plane is much weaker than the E field in Fig. 14 (a) (however the source is still present at the same location, due to the radiation directly from the physical layer interface IC, which is placed right beneath the optical module). The estimated radiated power is -96.9 dBm, which is about 14 dB lower than the radiated power calculated with pair # 3 working.

The measurement of the total radiated power (TRP) in the RC is performed to obtain the TRP reduction at frequency # 11 after removing pair # 3, which also turns out to be close to 14 dB. The estimated power through the scanning plane and the measured TRP in the RC before and after removing the radiated module are shown in TABLE 1. The power reductions of the estimated power and the measured TRP are fairly close, which further verifies that pair # 3 is the corresponding radiation source. The errors for the absolute values of the TRP are 3-4 dB.

5. CONCLUSION

Sparse ESM technique can be used to quickly localize major radiation sources in a complex system, which is a powerful and efficient tool for EMI debugging applications.

Typical sparse scanning time is 5-20 minutes as opposed to several hours for the uninform scan. Besides, radiated power through the scanning plane can be calculated from sparse scan using nearest neighbor interpolation method, which provides good repeatability within 1 dB and absolute accuracy of 3-4 dB. The ability to perform ESM transformation in real time allows accommodating the scanning strategy to a particular field distribution created by the DUT to further improve the convergence and hence decrease the scanning time. Radiated power estimation allows correcting the amplitude of the reconstructed image during the sparse scan and keeping it nearly constant regardless of the number of samples.

It was shown that the signal to noise ratio of the image is equal to the number of sparse samples for an idealized point source. In real applications the SNR is approximately proportional to the number of samples, allowing the estimation of the required number of samples to achieve a desired SNR. The image quality can be further improved if the samples are collected more densely at the locations where the field intensity is large.

Several criteria can be used to assess the quality of the acquired image. The quality of the image can be assessed by the power convergence plot (see Fig. 11 (h) for example). When the variation of the radiated power drops below a certain limit it can be concluded that the image is acquired with the comparable accuracy.

Another way to determine the image quality is to observe the changes in the real-time ESM image as new samples are being added. If there is no visible change in the image anymore, it means that enough samples are collected.

In summary, the proposed methodology is efficient and reliable in identifying major radiation sources, allowing to determine their location and relative strength along with the total radiated power on the DUT in real time during the scan. The weaker sources might be overwhelmed by the sparse sampling noise but the SNR estimation formula (16) allows estimating the required number of samples to reveal them.

BIBLIOGRAPHY

[1]   D. Baudry, C. Arcambal, A. Louis, B. Mazari, and P. Eudeline, "Applications of the near-field techniques in EMC investigations," *IEEE Trans. Electromagn. Compat.*, vol. 49, no. 3, pp. 485–493, Aug. 2007.

[2]   X. Dong, S. Deng, T. Hubing, and D. Beetner, "Analysis of chip-level EMI using near-field magnetic scanning," in *Proc. Int. Symp. Electromagn. Compat.*, vol. 1, Aug. 2004, pp. 174–177.

[3]   X. Ren et al., "The impact of near-field scanning size on the accuracy of far-field estimation," in *Proc. IEEE Int. Symp. Electromagn. Compat.*, Aug. 2014, pp. 582–587.

[4]   J. J. Wang, "An examination of the theory and practices of planar near-field measurement," *IEEE Trans. Antennas Propag.*, vol. 36, no. 6, pp. 746–753, Jun. 1988.

[5]   P. Maheshwari, V. Khilkevich, D. Pommerenke, H. Kajbaf, and J. Min, "Application of emission source microscopy technique to EMI source localization above 5 GHz," in *Proc. IEEE Int. Symp. Electromagn. Compat.*, Aug. 2014, pp. 7–11.

[6]   P. Maheshwari, H. Kajbaf, V. V. Khilkevich, and D. Pommerenke, "Emission source microscopy technique for EMI source localization," *IEEE Trans. Electromagn. Compat.*, vol. 58, no. 3, pp. 729–737, Jun. 2016.

[7]   X. Jiao et al., "EMI mitigation with lossy material at 10 GHz," in *Proc. IEEE Int. Symp. Electromagn. Compat.*, Aug. 2014, pp. 150–154.

[8]   K. S. Farhat and N. Williams, "Microwave holography applications in antenna development," in *Proc. IEE Colloquium Novel Antenna Meas. Technol.*, Jan. 1994, pp. 3/1–3/4.

[9]   P. L. Ransom and R. Mittra, "A method of locating defective elements in large phased arrays," *Proc. IEEE*, vol. 59, no. 6, pp. 1029–1030, Jun. 1971.

[10]   J. J. Lee, E. M. Ferren, D. P. Woollen, and K. M. Lee, "Near-field probe used as a diagnostic tool to locate defective elements in an array antenna," *IEEE Trans. Antennas Propag.*, vol. 36, no. 6, pp. 884–889, Jun. 1988.

[11]   M. Fallahpour, M. T. Ghasr, J. T. Case, and R. Zoughi, "A Wiener filterbased synthetic aperture radar algorithm for microwave imaging of targets in layered media," *Mater. Eval.*, vol. 69, no. 10, pp. 1227–1237, 2011.

[12]   D. M. Sheen, D. L. McMakin, and T. E. Hall, "Three-dimensional millimeter-wave imaging for concealed weapon detection," *IEEE Trans. Microwave Theory Technol.*, vol. 49, no. 9, pp. 1581–1592, Sep. 2001.

[13]   J. T. Case, M. T. Ghasr, and R. Zoughi, "Optimum two-dimensional uniform spatial sampling for microwave SAR-based NDE imaging systems," *IEEE Trans. Instrum. Meas.*, vol. 60, no. 12, 3806–3815, Dec. 2011.

[14] J. T. Case, M. T. Ghasr, and R. Zoughi, "Nonuniform manual scanning for rapid microwave nondestructive evaluation imaging," *IEEE Trans. Instrum. Meas*., vol. 62, no. 5, 1250–1258, May 2013.

[15] J. T. Case,M. T. Ghasr, and R. Zoughi, "Optimum 2-D nonuniform spatial sampling for microwave SAR-based NDE imaging systems," *IEEE Trans. Instrum. Meas*., vol. 61, no. 11, pp. 3072–3083, Nov. 2012.

[16] J. Song, Q. H. Liu, K. Kim, and W. R. Scott, "High-resolution 3-D radar imaging through nonuniform fast Fourier transform (NUFFT)," *Commun. Computat. Phys*., vol. 1, no. 1, pp. 176–191, 2006.

[17] H. Kajbaf, J. T. Case, Z. Yang, and Y. R. Zheng, "Compressed sensing for SAR-based wideband three-dimensional microwave imaging system using non-uniform fast Fourier transform," *IET Radar, Sonar Navigat*., vol. 7, no. 6, pp. 658–670, 2013.

[18] L. Le Cam, "The central limit theorem around 1935," *Statist. Sci*., vol. 1, 1986, pp. 78–91.

[19] J. A. Parker, R. V. Kenyon, and D. E. Troxel, "Comparison of interpolating methods for image resampling," *IEEE Trans. Med. Imaging*, vol. 2, no. 1, pp. 31–39, Mar. 1983.

[20] Q. Du, V. Faber, and M. Gunzburger, "Centroidal Voronoi tessellations: Applications and algorithms," *SIAM Rev*., vol. 41, no. 4, pp. 637–676, 1999.

[21] G. Koepke and J. Ladbury, "Radiated power measurements in reverberation chambers," in *Proc. 56th ARFTG Conf. Digest-Fall*, vol. 38, Nov. 2000, pp. 1–7.

[22] Q. Liu et al., "Modeling absorbing materials for EMI mitigation," in *Proc. IEEE Int. Symp. Electromagn. Compat*., Aug. 2015, pp. 1548–1552.

II. EMI COUPLING PATHS AND MITIGATION IN OPTICAL TRANSCEIVER MODULES

ABSTRACT

Optical transceiver modules are commonly used in telecommunication and data communication systems, and are among the most troublesome electromagnetic interference (EMI) problems for regulatory compliance at their operation frequencies and/or harmonics. In this work, simulations and measurements are performed on an optical sub-assembly (OSA) module, including the silicon photonics submodule assembly, in order to identify and characterize the EMI coupling paths. The total radiated power (TRP) is measured and computed. Through simulation and corroborating measurements, the dominant EMI coupling paths at high frequencies above 10 GHz are identified and characterized, and currents on the silicon photonic sub-assembly conductor housing and optical fiber connection ferrule are a dominant radiating source. EMI mitigation methods are developed and shown to be effective in reducing the radiated emissions from real product hardware.

1. INTRODUCTION

The continuous increase of data rate in electronic products and network bandwidth has resulted in the widespread use of optical transceiver modules in Gigabit Ethernet systems, due to their high throughput of several hundred gigabits per second (Gbps). These modules are typically used in high-end and low-end switches and routers, and are located at the front-end of the system chassis. Electromagnetic interference (EMI) problems can result from these modules at their operation frequency and/or harmonics [1] – [5]. The entire optical link of the module includes the line card printed circuit board (PCB), the optical cage connector, the connector housing/cage, the transceiver module, and the optical cable as shown in Fig. 1. The cage connector, the optical transceiver module and the optical cable ferrule have been identified as the main coupling paths or contributors of radiation at the front panel [6]. The EMI coupling paths of the cage connector and the EMI mitigation

of coupling from the connector using absorbing material have been discussed in detail [7]. Additionally, several electromagnetic shielding methods have been developed to mitigate EMI issues on the optical transceiver modules [8] – [10]. An EBG structure on the transceiver chassis has been proposed to suppress the EMI from the front of the module [11].

In order to further quantitatively investigate the EMI coupling paths on the optical transceiver module, measurements and full-wave simulations were performed on the optical subassembly package to compare total radiated power (TRP) variations with absorbing material covering different regions [1]. The FSV technique was used to compare the simulated and measured data. The comparison of the contributions to TRP from different parts of the signal path demonstrated that the connector from the transceiver circuit board to the flex cables in the OSA, and the flex cables connecting the transceiver circuit board to the electrical-to-optical interface assembly are two dominant coupling paths at high frequencies above 10 GHz [1]. This paper utilizes full-wave EM simulation to investigate the coupling paths that contribute to the propagating modes of the electromagnetic field within the cage that illuminates slots, and the silicon photonics conducting enclosure. The EMI coupling paths from these interior sources to the apertures on the outside enclosure and the electrical-to-optical interface assembly conductor packaging are demonstrated through simulation and measurement. Mitigation methods using absorbing materials to load the coupling paths are demonstrated to be effective in suppressing the radiation from the OSA. Application of absorbing material and conducting O-rings to mitigate the radiated emissions from real products provides corroboration for the identified EMI coupling paths as well as the EMI mitigation methods for the optical transceiver modules in real product applications.

The OSA features and geometry are given in Section II [1], and the TRP comparisons between measurement and simulation are shown for aspects of the OSA to support the simulation models used in identifying coupling paths and mitigation approaches. EMI coupling paths and the mitigation methods are analyzed and evaluated through simulation in Section III. In Section IV, several EMI mitigation methods that can reduce the radiated emissions in real products are presented.

2. SILICON OPTICAL SUBASSEMBLY PACKAGE

2.1. Optical Subassembly (OSA) Module Structure

A schematic diagram of a typical optical link at the front of the chassis is shown in Fig. 1. The connector shield cage located on the line card PCB encloses the cage connector and the transceiver module.

The signal is transmitted through the cage connector from the line card to the transceiver circuit board. The signal on the transceiver circuit board is connected to the silicon photonic subassembly through a section of flex cables. The electrical-to-optical (and vice versa) interface assembly is an electro-optical data converter, which includes the silicon photonics, with intelligent controller and data processor and converts the electrical signal into an optical signal.
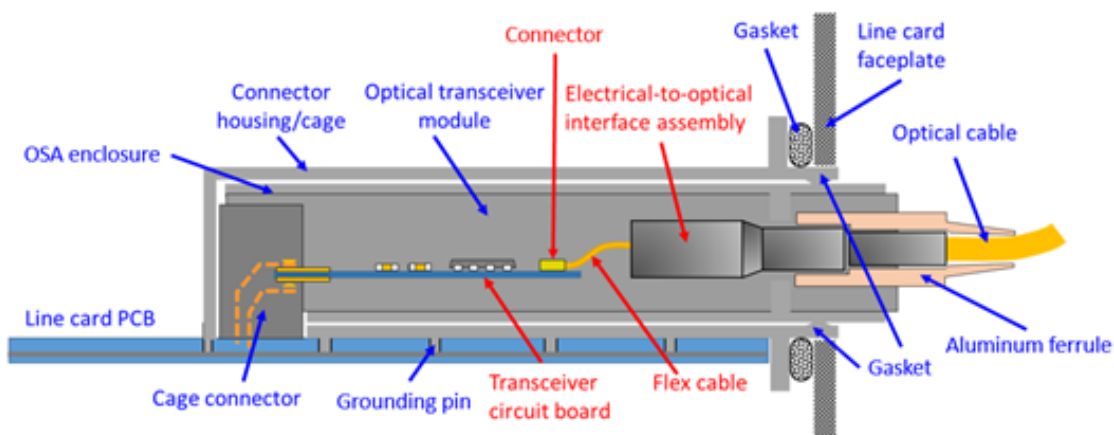

Figure 1. Diagram of the entire link of the optical transceiver module.

In the end, the optical signal is transmitted to other devices through an optical fiber cable. It is the aluminum ferrule on the optical fiber assembly that is inserted into the OSA that is the radiating EMI antenna that is among the most troublesome EMI problems in meeting regulatory requirements with these OSAs.

2.2. OSA Test Board and Simulation Model

A test board including the flex cables and the electrical-to-optical interface assembly, which is shown in Fig. 2 (a), has been designed to focus on the coupling paths and radiation from the flex cables, the connector on the transceiver circuit board, and the electrical-to-optical interface of the module [1]. On the test board, two striplines are used as the differential signal input. Precision 2.4 mm connectors are mounted on the bottom of the board and back-drilling is used for the board to facilitate a sufficiently smooth impedance transition to enable operation up to 30 GHz. In the measurement, one of the 2.4 mm connectors at the bottom of the board is connected to one port of the VNA as the signal source. The other connector is terminated with 50Ω. This board mimics the transceiver PCB in the optical module. The corresponding simulation model, which is shown in Fig. 2 (b), is created in CST Microwave Studio [12]. Accordingly, in the simulation model, only one single stripline is excited from one connector on the bottom of the board. The metal in the module is approximated and characterized as perfect electric conductor (PEC). The dielectric material around the flex cables (in red color) has a relative permittivity of 3.4 and loss tangent of 0.01 at 10 GHz, while the dielectric material for the circuit substrate inside the electrical-to-optical interface (in green color) has a relative permittivity of 9.2 and loss tangent of 0.003 at 10 GHz.

There are nine circuit layers inside the electrical-to-optical interface module, among which there is a signal layer and eight ground or power planes. The geometry of the signal layer is shown in Fig. 2(c), which has four pairs of differential signal traces connected with the four pairs of flex cables. In real products, the signal traces in the signal circuit layer are connected with the silicon photonics component, which converts the electrical signal into an optical signal. However, the details of the silicon photonics part could not be obtained due to it being proprietary. Therefore, the signal traces in the electrical-to-optical interface module are terminated with 300Ω impedance, which is used to roughly represent the connection with the silicon photonics and simplify the model. The value of 300Ω was found from TDR measurements into the optical subassembly, though there is considerable uncertainty in this value.

(a)

(b)

(c)
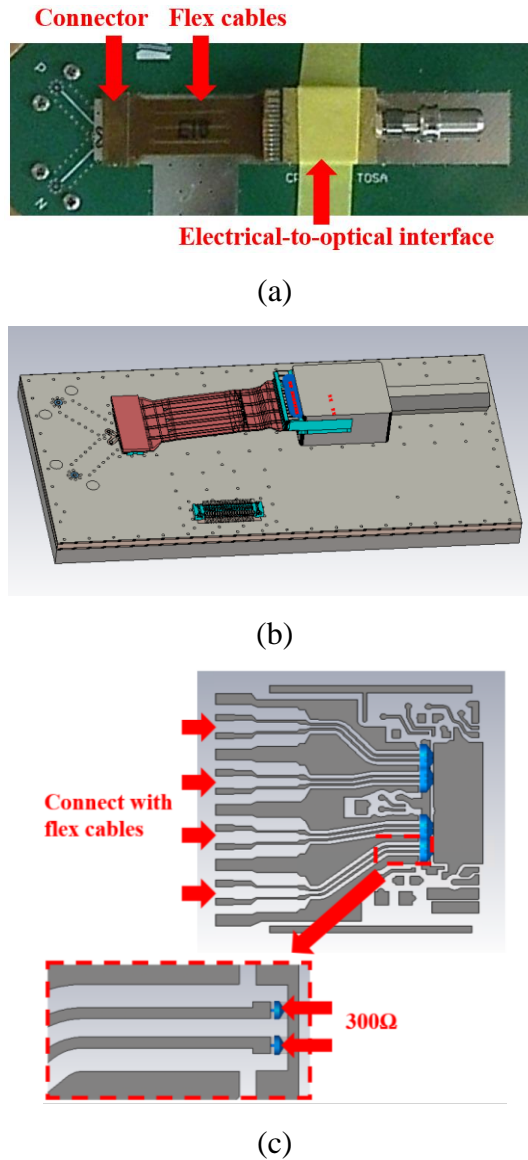
Figure 2. Optical sub-assembly test board. (a) Experimental test setup. (b) The corresponding simulation model. (c) The interior signal circuit layer of the electrical-to-optical interface which has four pairs of differential traces connected with the flex cables. Every single signal trace in the circuit layer is terminated with 300Ω impedance in the simulations.

In order to validate the simulation model and quantify the TRP contribution of the OSA module, TRP results from measurement and simulation were compared [1],[13], as shown in Fig. 3. In the measurement, the TRP of the OSA module in Fig. 2 (a) was obtained through a mode-stirred reverberation chamber (RC) method [14], [15].
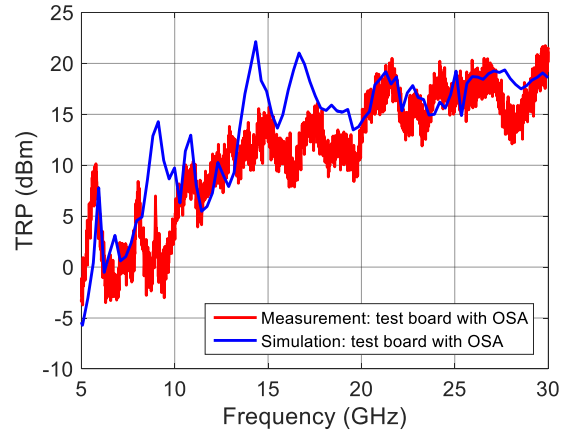
Figure 3. TRP comparison between measurement and simulation of the test board with OSA model as shown in Fig. 2.

Table 1. GRADE and SPREAD values of Fig. 3, 85% threshold.

	GRADE	SPREAD
ADM	5 (poor)	3 (good)
FDM	5 (poor)	4 (fair)
GDM	5 (poor)	3 (good)

The FSV method is used herein to assess the similarity between the measurements and simulations. The FSV has three figures of merit for the comparison of two data sets: ADM (Amplitude Difference Measure), FDM (Feature Difference Measure), and GDM (Global Difference Measure) [16] - [18]. For each figure of merit, two quality factors are considered - GRADE and SPREAD. The GRADE is an indication of the quality of the comparison, and the SPREAD indicates the level of the reliability of the outputs. The numerical values are calculated to be from 1 to 6 and assessed as excellent, very good, good, fair, poor, very poor. The FSV method is applied to compare the simulations with the measurements as shown in Fig. 3, and the GRADE and SPREAD values are listed in TABLE 1, in which the threshold value of 85% is used. Even though the GRADE values are poor, the SPREAD values turn out to be good, which indicates good reliability of the results.

Differences of approximately 5-10 dB between simulation and measurement are apparent at 9 GHz, 14 GHz, and 17 GHz as seen in Fig. 3. One reason for the discrepancy may be due to incomplete information of proprietary details of the structure that includes the transition structure between the flex cables and the electrical-to-optical interface assembly, and the input impedance looking into the terminals of the electrical-to-optical silicon photonics component. Another possible discrepancy might be the characterization of the dielectric material inside the electrical-to-optical interface. However, given the complexity of the geometry of the connector and interconnect transitions, the electrical-to-optical interface circuit and package, and the challenges in making good measurements, the comparison is sufficient in the present case for EMI coupling path and mitigation discovery.

2.3. Apply Absorbing Material on the Module

The OSA module can be roughly separated into three parts: the striplines and the connector on the test board, the flex cables, and the electrical-to-optical interface assembly. To quantify the radiation from each part individually, the reductions of TRP by placing absorbing material on each part were compared. Absorbing material ECCOSORB BSR-2 [19] from Laird Technology was used in the experiments. The permittivity and permeability of the material from 1 to 18 GHz were obtained from Laird, and the parameters from 18 to 30 GHz were curved fitted and extrapolated using a polynomial formulation in CST Microwave Studio [1].

Fig. 4(a) and Fig. 4(b) show the module experimental configuration and the simulation model after adding absorbing material BSR-2 of 1 mm thickness to cover the entire OSA module as shown. From the TRP measurement results in Fig. 4 (c), significant TRP reduction is achieved above 10 GHz. The reduction in TRP after applying absorbing material is shown in Fig. 4 (d). The FSV method has also been applied on Fig. 4 (d) to compare the measurement and simulation data, and the GRADE and SPREAD values indicate a good reliability of the results as well, as shown in TABLE II.

Absorbing material was also used on the three parts individually to compare their contributions to the TRP, and the simulation and measurement results both indicate that the connector and the flex cables are two dominant radiation sources above 10 GHz [1].

The conclusion in [1] gives a critical guidance on the analysis of the EMI coupling paths in the optical transceiver module, which will be further verified and studied in the following parts through different measurement and simulation scenarios.

Table 2. GRADE and SPREAD values of Fig. 4(d), 85% threshold.

	GRADE	SPREAD
ADM	5 (poor)	3 (good)
FDM	5 (poor)	4 (fair)
GDM	5 (poor)	3 (good)

(a)   (b)

(c)   (d)
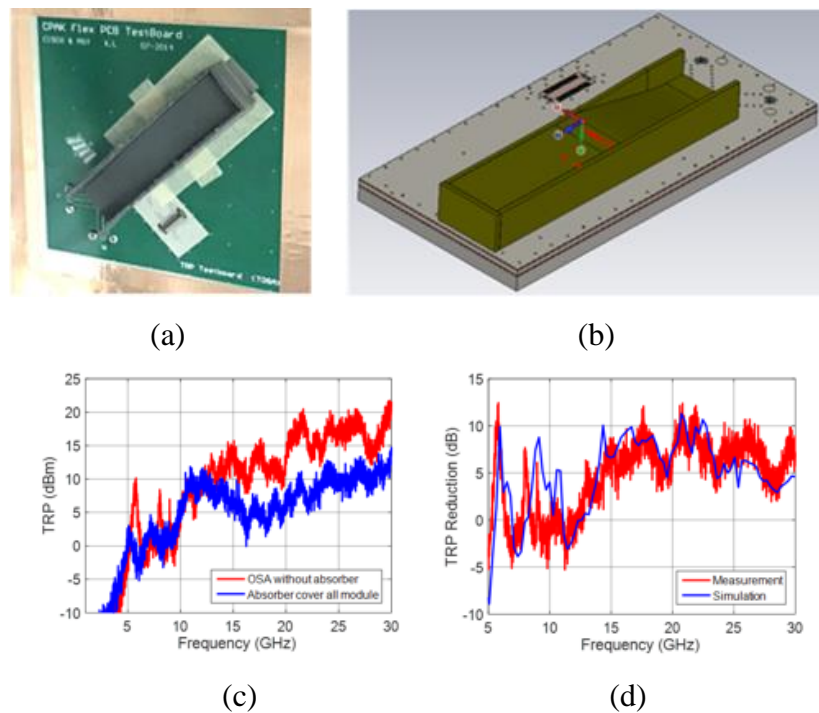
Figure 4. Comparison between measurement and simulation after adding absorbing material on the whole OSA module. (a) The OSA test board covered by the absorbing material of 1mm thickness. (b) The simulation OSA test board covered by the absorbing material of 1mm thickness. (c) Comparison of TRP measurement with and without absorbing material. (d) Comparison of TRP reduction after adding absorbing material between measurement and simulation.

3. EMI COUPLING PATH CHARACTERIZATION AND MITIGATION

3.1. EMI Coupling Paths Analysis in Simulation

The interior of a production optical transceiver module is shown in Fig. 5, in which there are two individual modules – transmitter optical sub-assembly (TOSA) module and receiver optical sub-assembly (ROSA) module. The TOSA converts the electrical signal arriving from the transceiver circuit board to an optical signal and transmits the optical signal to other devices, while the ROSA works in the receive direction of the signal. Since the interior structure of the ROSA cannot be acquired due to its proprietary nature, only the model of the TOSA is used in this paper for the analysis of EMI coupling paths in the absence of the ROSA in full-wave simulation.

To study the EMI coupling paths from the inside sources to the space outside the enclosure, the simulation model of the TOSA was augmented to include the shielding enclosure of the TOSA as in the production hardware. At first, only the enclosure bottom was added to the model, as shown in Fig. 6 (a). The enclosure material is characterized as PEC, while the transceiver circuit board is approximated to be PEC as well to simplify the model. The dielectric material above the transceiver circuit board has a relative permittivity of 4.5. Similar to the previous model without the enclosure, only one single stripline that is closest to the enclosure side is excited directly on the transceiver circuit board (which is just a piece of PEC board). Thus, the radiation from the transceiver circuit board is not considered in this simulation.

The optical transceiver module has two working modes at 25.78 GHz and 27.95 GHz, causing serious EMI issues at these two frequencies. However, all the following EMI analysis will focus on 25.78 GHz only. The EMI behavior at 27.95 GHz is similar to 25.78 GHz.

The surface current distribution at 25.78 GHz is shown in Fig. 6 (b). It can be seen that the surface current is mainly distributed on the flex cables as expected, and there is nearly no surface current on the metal of the electrical-to-optical interface assembly, which agrees with the conclusion in [1].

In order to study the EMI coupling paths from the intended signal on the interior to the space exterior to the electrical-to-optical interface assembly enclosure, the top of the

OSA enclosure is added in the simulation model of Fig. 6 (a), as shown in Fig. 7 (a). The right side of the module in Fig. 5 is inserted into the shielding cage with the cage connector. In the simulation model, it is closed with a PEC in order to study the coupling path and radiation from the optical output end that is not contained within the overall enclosure of the networking equipment.
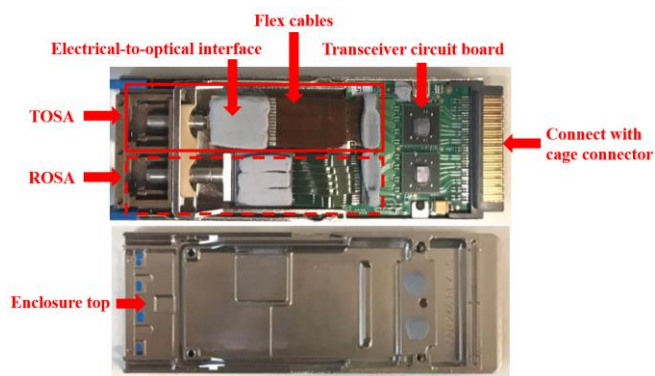
Figure 5. Interior of a production optical transceiver module.

There is a gap between the cylindrical metal port that egresses the OSA module and the enclosure as shown in Fig. 7(b). The optical cable plugs in to this port. Experimental work with the production hardware showed that there is some leakage due to a gap around the mechanical handle insertion areas of the enclosure, as shown in Fig. 7 (b). These locations were demonstrated experimentally in the production hardware to be the primary leakage points.

The surface current is again used for the analysis of EMI coupling paths inside the enclosure. The surface current distribution at 25.78 GHz is shown in Fig. 7 that shows illumination and coupling to the exterior surface of the electrical-to-optical interface assembly. The surface current distribution at 27.95 GHz is similar and is omitted.

The surface current distribution on the exterior of the electrical-to-optical interface assembly when the enclosure top is added in the model is depicted and identified in Fig. 7 (c), and it is this current that is also continued on to the conducting cylinder that is part of the assembly and into which the optical fiber is inserted. These currents as seen looking into the cylinder from the fiber insertion point are seen through the gap and on the cylinder in Fig. 7 (e). This metal cylinder egresses the OSA shielding enclosure and is not

electrically well connected to the enclosure. Together with the aluminum ferrule of the optical fiber cable which inserts into the TOSA port, a monopole antenna is formed with the ferrule and the large equipment shielding enclosure that is an effective EMI antenna at gigahertz frequencies. Further, since typically a piece of networking equipment will have tens or hundreds of such ports, this is among the primary EMI challenges in meeting compliance standards for such equipment.

(a)

(b)   (c)
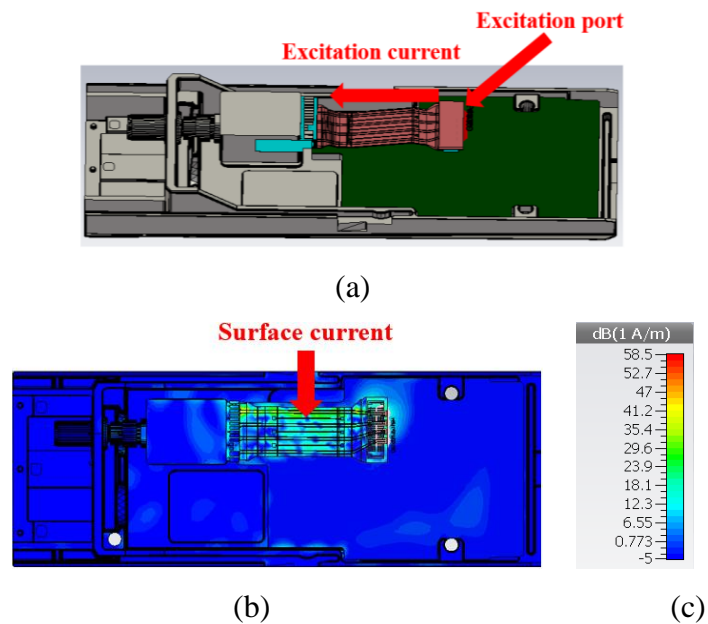
Figure 6. (a) OSA simulation model only without the enclosure top. (b) Surface current distribution at 25.78 GHz in top view.

There is also considerable surface current on the enclosure cover as shown in Fig. 7 (d). The enclosure cavity provides an EMI coupling path for propagating modes that can illuminate slots and seams in the OSA enclosure, e.g., the mechanical handle assembly on the sides as identified in Fig. 7 (b). The surface currents illuminating these seams are shown in Fig. 7 (c) and Fig. 7 (d). Experiments with the production hardware during compliance testing showed these leakage points to be significant. The coupling to the cavity modes within the enclosure can come from the flex cables and the cage connector [7].
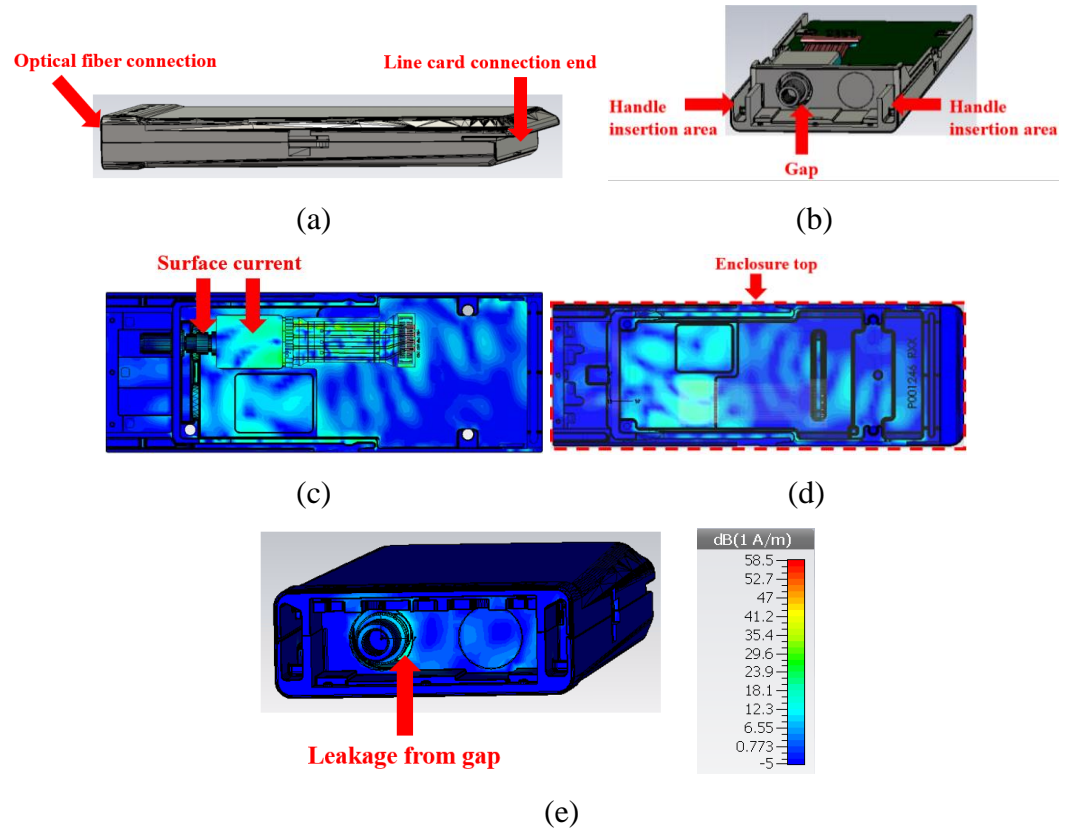
Figure 7. (a) Simulation model for the optical transceiver module, enclosed in a complete enclosure. (b) The positions of the handle insertion area and the gap between the cylindrical metal part and the enclosure. (c) Surface current distribution on the OSA module and the enclosure bottom, with the enclosure top being hidden. (d) Surface current distribution on the OSA module and the enclosure top, with the enclosure bottom being hidden. (e) Surface current distribution on the enclosure surface in front view, and the magnitude scale of the surface current distribution.

3.2. EMI Mitigation with Absorbing Material

The dominant EMI coupling paths in the optical assembly and the leakage points in the enclosure have been determined and can provide direction for applying EMI mitigation strategies. Absorbing material having the properties of the Laird ECCOSORB BSR-2 was used in full-wave simulation to evaluate the TRP reduction for several locations of absorbing material.

The simulation model without absorber and with the enclosure top present but hidden is shown in Fig. 8(a). A 26 mm × 16 mm piece of BSR-2 absorbing material of 1 mm thickness was added to the bottom side of the enclosure lid and located above the flex

cables (but not in contact with the flex cables), as shown in Fig. 8(b). In an additional step, absorbing material was added to the gap between the cylindrical metal egress of the electrical-to-optical module and the enclosure, as well as the leakage locations on the two mechanical handle insertion areas of the enclosure, as shown in Fig. 8(c). Finally, using the model of Fig. 8(a), absorbing material of 0.5 mm thickness was added to cover the metal of the electrical-to-optical interface and the metal cylinder inside the enclosure, as shown in Fig. 8(d), to further verify the EMI coupling paths and quantify a potential mitigation approach.
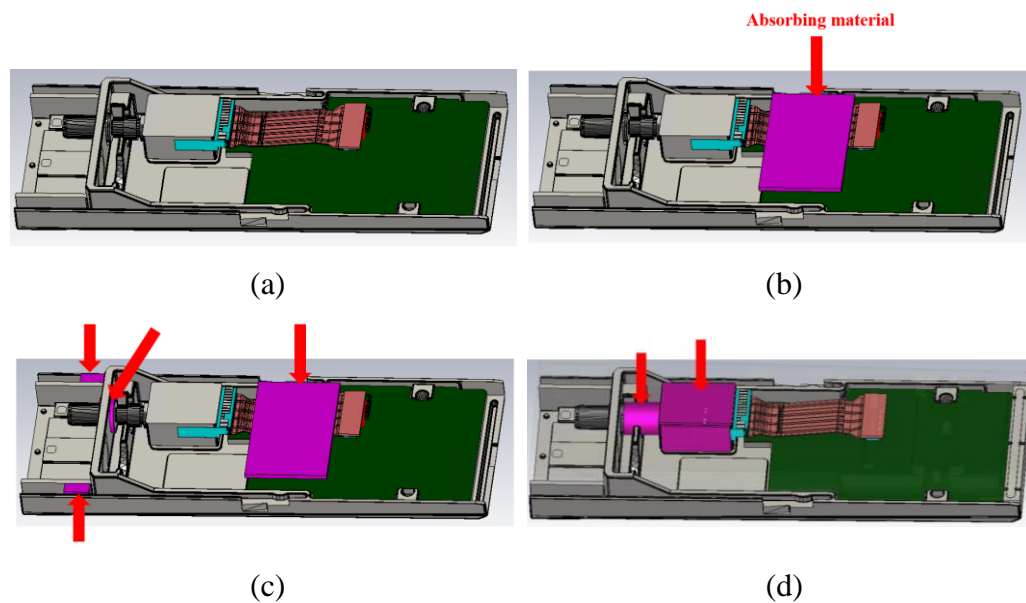
Figure 8. (a) Simulation model with closed enclosure (enclosure top being hidden) and without absorber. (b) Simulation model with closed enclosure, and absorbing material with dimensions of 26mm × 16mm and thickness of 1 mm on the enclosure lid underside above the flex cables. (c) Simulation model with closed enclosure with absorbing material of 1 mm thickness on the enclosure top above the flex cables, and to the space between the cylindrical metal part of the electrical-to-optical module and the enclosure, as well as the leakage space on the two handle sides of the enclosure. (d) Simulation model with closed enclosure, and absorbing material with thickness of 0.5mm on the metal of the electrical-to-optical interface assembly and the metal cylinder inside the enclosure.

The reductions in TRP for the two cases using absorbing material are given in Table 3. A reduction in the TRP of 4-7 dB results at the two frequencies of concern after adding absorbing material on the underside of the enclosure lid above the flex cables. After adding

absorbing material to the cylindrical egress of the electrical-to-optical module, and the handle insertion areas, the TRP is further reduced 2-3 dB.

The TRP is significantly reduced 8-9 dB after adding absorbing material on the metal of the electrical-to-optical interface and the cylinder as shown in Fig. 8(d), and the surface current magnitude on the metal where the absorbing material was added (not shown here) is reduced by greater than 10 dB.

Table 3. TRP results in simulation of Fig. 8.

Simulated TRP (dBm)	25.78 GHz	27.95 GHz
Model in Fig. 8(a)	-14.9 dBm	-17.3 dBm
Model in Fig. 8(b)	-22.5 dBm	-21.3 dBm
(Compared to Fig. 8(a))	(7.6dB reduction)	(4dB reduction)
Model in Fig. 8(c)	-25.3 dBm	-23.0 dBm
(Compared to Fig. 8(a))	(10.4dB reduction)	(5.7dB reduction)
Model in Fig. 8(d)	-24 dBm	-25.3 dBm
(Compared to Fig. 8(a))	(9.1dB reduction)	(8dB reduction)

4. EMI MITIGATION IN THE PRODUCTION HARDWARE

The simulation and experimental results in the previous sections have demonstrated the EMI coupling paths and the leakage points of the enclosure, and potential corresponding mitigation methods. Measurements on a networking equipment product using multiple optical transceiver modules were performed for EMI compliance that support the conclusions for the EMI coupling paths herein, as well as the proposed mitigation approaches using absorbing material.

In the product networking equipment testing one chassis with functioning optical transceiver modules with data traffic did not meet the FCC Class A limit plus required margin at 25.78 GHz and 27.95 GHz, due to radiation from the optical transceiver modules. For example, one measurement showed that when one line card was working with four

optical transceiver modules inserted, it passed the FCC Class A limit by 0.4 dB with no margin typically required in product applications.
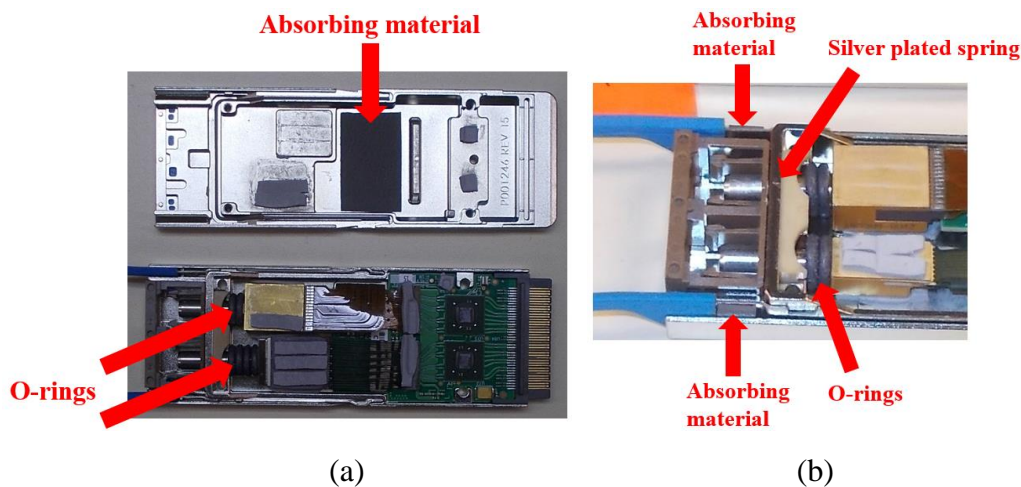

Figure 9. EMI mitigation methods in the production hardware. (a) Adding absorbing material inside the enclosure above the flex cables, and adding grounding O-rings around the cylindrical metal portion of the electrical-to-optical module. (b) Adding some silver plated spring around the cylindrical metal, and adding absorbing material on the handles on two sides.

Afterwards, the mitigation approaches applied to the coupling paths and demonstrated in the simulation of the previous section shown in Fig. 8 were utilized in the optical transceiver modules. An absorbing material rectangle with dimensions of 26mm $\times$ 16mm and thickness of 1 mm was added above the flex cables and the bottom side of the OSA enclosure lid as shown in Fig. 9(a) [20], [21]. Then, conducting elastomer O-rings surrounding the cylindrical metal egress of the electrical-to-optical module were further added for grounding as shown in Fig. 9 (a) and Fig. 9(b). Further, silver plated springs surrounding the cylindrical metal egress structure were added as well as absorbing material around the mechanical handle insertion areas as indicated in Fig. 9(b).

The reduction in measured radiated emissions from two line cards working normally with eight optical transceiver modules inserted after applying the mitigation methods as shown in Fig. 9 is given in Table 4. Though the A/B comparison of the networking equipment with four OSA modules is not available, the reduction with eight

OSA modules using the EMI mitigation approaches indicated in Table 3 with the production networking equipment supports the EMI coupling paths and mitigation approaches in the previous section.

Table 4. Mitigation of radiated emissions.

Difference with FCC Class A limit (dB)	25.78 GHz	27.95 GHz
Adding absorbing materials + O-rings (2 line cards, 8 modules)	-8 dB	-4 dB
Adding absorbing materials + O-rings + silver plated spring seal + absorbing materials on handles (2 line cards, 8 modules)	-15 dB	-9 dB

5. CONCLUSION

EMI coupling paths in an optical sub-assembly for high-data-rate networking equipment have been demonstrated herein. Further, a methodology using numerical simulation with corroborating experiments has been shown that can be used for discovery and design, or identification of EMI coupling paths and EMI mitigation.

The EMI coupling paths demonstrated in the OSA are the cage connector [7], the connector between the transceiver circuit board and the flex cables, and the flex cables. The OSA module enclosure provides a cavity-like structure for the EMI coupling paths to illuminate the electrical-to-optical module conductor housing that contains the silicon photonics. The conducting housing of the electrical-to-optical module egresses the OSA enclosure without a good electrical connection to the OSA enclosure. The optical fiber plugging into the OSA has an aluminum ferrule for mechanical robustness that extends nearly 3 cm beyond the networking equipment enclosure and forms a radiating monopole antenna. With many tens, or hundreds of these in an equipment rack, the EMI can surpass regulatory limits. EMI mitigation using absorbing material around the cage connector or in

the OSA enclosure above the flex cable was demonstrated to be highly effective, and using absorbing material on the OSA housing can mitigate the radiation from the currents on the OSA and aluminum ferrule on the fiber cable. Further, conducting elastomer O-rings can be utilized for grounding the electrical-to-optical housing to the OSA enclosure to reduce emissions. In the actual product application, several elastomer O-rings were used, in addition to absorbing material in the OSA enclosure above the flex cable and in the handle insertion areas.
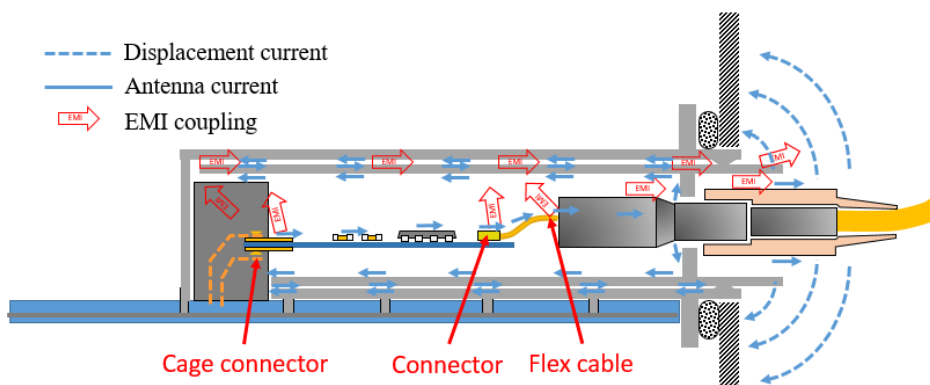

Figure 10. Summary of the EMI coupling paths in the optical transceiver module.

BIBLIOGRAPHY

[1]   J. Li, X. Li, X. Jiao, S. Toor, L. Zhang, A. Bhobe, J. Drewniak, and D. Pommerenke, "EMI coupling paths in silicon optical sub-assembly package," *2016 IEEE International Symposium on Electromagnetic Compatibility (EMC)*, pp. 890–895, Jul. 2016.

[2]   T. Wu, W. Jou, S. Dai, and W. Cheng, "Effective electromagnetic shielding of plastic packaging in low-cost optical transceiver modules," *Journal of Lightwave Technology*, vol. 21, no. 6, pp. 1536–1543, 2003.

[3]   H. Oomori, M. Shiozaki, and H. Kurashima, "Development of a practical electro-magnetic interference (EMI) simulation in high speed optical transceivers," *2009 59th Electronic Components and Technology Conference*, pp. 1908–1913, 2009.

[4]   D. Kawase, H. Oomori, M. Shiozaki, and H. Kurashima, "EMI suppression of 10Gbit/s optical transceiver by using EBG structure," *2011 IEEE International Symposium on Electromagnetic Compatibility*, pp. 33–38, 2011.

[5]   W. Cheng, W. Hung, C. Lee, G. Hwang, W. Jou, and T. Wu, "Low-Cost and Low-Electromagnetic-Interference Packaging of Optical Transceiver Modules," *Journal of Lightwave Technology*, vol. 22, no. 9, pp. 2177–2183, 2004.

[6]   J. Li, S. Toor, A. Bhobe, J. L. Drewniak, and J. Fan, "Radiation physics and EMI coupling path determination for optical links," *2014 IEEE International Symposium on Electromagnetic Compatibility (EMC)*, pp. 576–581, Aug. 2014.

[7]   J. Li, X. Li, S. Toor, H. Fan, A. U. Bhobe, J. Fan, and J. L. Drewniak, "EMI Coupling Paths and Mitigation in a Board-to-Board Connector," *IEEE Transactions on Electromagnetic Compatibility*, vol. 57, no. 4, pp. 771–779, Aug. 2015.

[8]   W. Cheng, T. Wu, W. Jou, "Electromagnetic shielding of plastic packaging in cost-effective optical transceiver modules," *in Lasers and Electro-Optics Society*, *The 16th Annual Meeting of the IEEE*, vol. 2, pp. 565-566, Oct. 2003.

[9]   T. Wu, W. Hung, C. Lee, C. Lin, W. Jou, W. Cheng, "A low-cost plastic package for 2.5Gbps optical transceiver module with high electromagnetic shielding," *in 54th Electronic Components and Technology Conference Proceedings*, vol. 1, pp. 199-202, June 2004.

[10]   T. Wu, W. Jou, S. G. Dai, W. Cheng, "Effective electromagnetic shielding of plastic packaging in low-cost optical transceiver modules," *in Lightwave Technology, Journal of* , vol. 21, no. 6, pp. 1536-1543, June 2003.

[11]   D. Kawase, H. Oomori, M. Shiozaki, H. Kurashima, "EMI suppression of 10Gbit/s optical transceiver by using EBG structure," *in Electromagnetic Compatibility (EMC), 2011 IEEE International Symposium on* , pp. 33-38, Aug. 2011.

[12]   CST MICROWAVE STUDIO, CST Computer Simulation Technology, Available: https://www.cst.com/.

[13]   G. Li, G. Hess, R. Hoeckele, S. Davidson, P. Jalbert, V. V. Khilkevich, T. P. V. Doren, D. Pommerenke, and D. G. Beetner, "Measurement-Based Modeling and Worst-Case Estimation of Crosstalk Inside an Aircraft Cable Connector," *IEEE Transactions on Electromagnetic Compatibility*, vol. 57, no. 4, pp. 827–835, 2015.

[14]   C. L. Holloway, H. A. Shah, R. J. Pirkl, W. F. Young, D. A. Hill, and J. Ladbury, "Reverberation Chamber Techniques for Determining the Radiation and Total Efficiency of Antennas," *IEEE Transactions on Antennas and Propagation*, vol. 60, no. 4, pp. 1758–1770, 2012.

[15]   Q. Liu, X. Jiao, J. Li, V. Khilkevich, J. Drewniak, P. Dixon, and Y. Arien, "Modeling absorbing materials for EMI mitigation," *2015 IEEE International Symposium on Electromagnetic Compatibility (EMC)*, Aug. 2015.

[16]   A. Duffy, A. Martin, A. Orlandi, G. Antonini, T. Benson, and M. Woolfson, "Feature Selective Validation (FSV) for Validation of Computational Electromagnetics (CEM). Part I—The FSV Method," *IEEE Transactions on Electromagnetic Compatibility*, vol. 48, no. 3, pp. 449–459, Aug. 2006.

[17]   A. Orlandi, A. Duffy, B. Archambeault, G. Antonini, D. Coleby, and S. Connor, "Feature Selective Validation (FSV) for Validation of Computational Electromagnetics (CEM). Part II— Assessment of FSV Performance," *IEEE Transactions on Electromagnetic Compatibility*, vol. 48, no. 3, pp. 460–467, Aug. 2006.

[18]   IEEE Standard P1597, Standard for Validation of Computational Electromagnetics Computer Modeling and Simulation – Part 1, 2 2008.

[19]   ECCOSORB®   BSR,   Laird   Technologies,   Available: http://www.eccosorb.com/products-eccosorb-bsr.htm.

[20]   G. Shen, Q. Liu, X. Jiao, R. He, V. Khilkevich, P. Dixon, Y. Arien, and M. Khorrami, "EMI control performance of the absorbing material for application on flexible cables," *2016 IEEE International Symposium on Electromagnetic Compatibility (EMC)*, pp. 30–35, Jul. 2016.

[21]   X. Jiao, P. Maheshwari, V. Khikevich, P. Dixon, Y. Arien, A. Bhobe, J. Li, X. Li, D. Pommerenke, J. Drewniak, H. Kajbaf, and J. Min, "EMI mitigation with lossy material at 10 GHz," *2014 IEEE International Symposium on Electromagnetic Compatibility (EMC)*, pp. 150–154, 2014.

2. CONCLUSION

In Paper I, the proposed Sparse ESM technique is efficient and reliable in identifying major radiation sources, allowing to determine their location and relative strength along with the total radiated power on the DUT in real time during the scan. The weaker sources might be overwhelmed by the sparse sampling noise but the SNR estimation formula (16) allows estimating the required number of samples to reveal them.

In Paper II, EMI coupling paths in an optical sub-assembly for high-data-rate networking equipment have been demonstrated. Mitigation methods using absorbing materials to load the coupling paths are demonstrated to be effective in suppressing the radiation from the OSA. Further, a methodology using numerical simulation with corroborating experiments has been shown that can be used for discovery and design, or identification of EMI coupling paths and EMI mitigation.

VITA

Ling Zhang received the B.S. degree in Electrical Engineering from Huazhong University of Science and Technology, Wuhan, China in June 2015. He received his M.S. degree in Electrical Engineering from Missouri University of Science and Technology, Rolla, MO, USA in December 2017.

His research interests included the Emission Source Microscopy Methodology for EMI product application and radiation analysis of the optical transceiver module.